A multi-tiered map of EMT defines major transition points and identifies vulnerabilities

Indranil Paul[1], Dante Bolzan[2], Ahmed Youssef[1], Keith A. Gagnon[3], Heather Hook[4], Gopal Karemore[5], Michael UJ Oliphant[6], Weiwei Lin[1], Qian Liu[7], Sadhna Phanse[1], Carl White[1], Dzmitry Padhorny[8], Sergei Kotelnikov[8], Guillaume P. Andrieu[9], Christopher S. Chen[3], Pingzhao Hu[7], Gerald V. Denis[10], Dima Kozakov[8], Brian Raught[11], Trevor Siggers[4], Stefan Wuchty[2†], Senthil K. Muthuswamy[6†], Andrew Emili[1,12†*]

Affiliations

[1] Department of Biochemistry, Boston University School of Medicine, Boston University, 72 East Concord Street, Boston, MA 02118, USA

[2] (a) Department of Biology, University of Miami, 1301 Memorial Drive, Coral Gables, FL 33146, USA; (b) Sylvester Comprehensive Cancer Center, 1475 NW 12th Ave, Miami, FL 33136, USA

[3] (a) Department of Biomedical Engineering, Boston University, 44 Cummington Mall, Boston, MA 02215, USA; (b) Biological Design Center, Boston University, 610 Commonwealth Avenue, Boston, MA 02215

[4] (a) Department of Biology, Boston University, 24 Cummington Mall, Boston, MA 02115, USA; (b) Biological Design Center, Boston University, 610 Commonwealth Avenue, Boston, MA 02215

[5] Advanced Analytics, Novo Nordisk A/S, 2760 Måløv, Denmark

[6] Cancer Research Institute, Department of Medicine, Beth Israel Deaconess Medical Center, Boston MA 02115, USA

[7] Department of Biochemistry and Medical Genetics, University of Manitoba, Winnipeg, Manitoba R3E 0J9, Canada

[8] (a) Department of Applied Mathematics and Statistics, Stony Brook University, 11794 Stony Brook, NY; (b) Laufer Center for Physical and Quantitative Biology, Stony Brook University, Stony Brook, New York, 11794, United States

[9] Team 2 - Institut Necker-Enfants Malades, INSERM U1151, Paris, France

[10] Boston Medical Center Cancer Center, Boston University, Boston University, 72 East Concord Street, Boston, MA 02118, USA

[11] Discovery Tower (TMDT), 101 College St, Rm. 9-701A, University of Toronto, Toronto, Ontario, M5G 1L7, Canada

[12] Department of Biology, Charles River Campus, Boston University, Life Science & Engineering (LSEB-602), 24 Cummington Mall, Boston, MA 02215 USA

† Co-communicating authors

*Correspondence to: aemili@bu.edu

Summary

Epithelial to mesenchymal transition (EMT) is a complex cellular program proceeding through a hybrid E/M state linked to cancer-associated stemness, migration and chemoresistance. Deeper molecular understanding of this dynamic physiological landscape is needed to define events which regulate the transition and entry into and exit from the E/M state. Here, we quantified >60,000 molecules across ten time points and twelve omic layers in human mammary epithelial cells undergoing TGFβ-induced EMT. Deep proteomic profiles of whole cells, nuclei, extracellular vesicles, secretome, membrane and phosphoproteome defined state-specific signatures and major transition points. Parallel metabolomics showed metabolic reprogramming preceded changes in other layers, while single-cell RNA sequencing identified transcription factors controlling entry into E/M. Covariance analysis exposed unexpected discordance between the molecular layers. Integrative causal modeling revealed co-dependencies governing entry into E/M that were verified experimentally using combinatorial inhibition. Overall, this dataset provides an unprecedented resource on TGFβ signaling, EMT and cancer.

Short title

Multi-level time-resolved deconstruction of EMT program

Keywords

TGFβ signaling, Epithelial to Mesenchymal Transition, EMT, Multi-omics, Mass Spectrometry, Proteomics, Single Cell RNA Sequencing, Multiplexed, Cancer

Introduction

Epithelial to mesenchymal transition (EMT) regulates cell plasticity during embryonic development, wound healing, fibrosis and cancer, where polarized epithelial (E) cells dedifferentiate, transition through intermediate hybrid states (E/M) and acquire mesenchymal (M) properties (Nieto et al., 2016). In cancer, cells in E/M state possess several clinically important attributes of circulating tumor cells (CTCs) and are responsible for EMT-associated stemness, chemoresistance, immune evasion and metastasis (Dongre and Weinberg, 2019). Complete molecular characterization of E/M states, and the mechanisms driving plasticity between E→E/M→M transitions will enable development of refined mechanistic models and discovery of new therapeutic strategies.

Approximately 150 genes are currently described as hallmarks of EMT (MSigDB database) that were identified from studies measuring the expression of 'endpoint' markers (e.g. CDH1, MUC1, VIM, FN1) to track the process (Sha et al., 2019). Although EMT is frequently studied as a transcriptionally-driven program (Yang et al., 2020), the poor correlation between genomic alterations or mRNA levels and proteins in tumors (Liu et al., 2016) highlights the need for multi-level analysis. Furthermore, EMT is likely an *emergent phenomenon*, where the shifts in cell physiology and phenotype are orchestrated by intra- and extra-cellular signaling (Sigston and Williams, 2017), extensive receptor-ligand crosstalk, protein relocalization (Hung and Link, 2011) and metabolic adaptations (Thomson et al., 2019) that requires an integrated multi-omic approach. However, most attempts made to model EMT primarily invoked gene-regulatory networks (GRNs) controlled by key transcription factors (TFs) and miRNAs. These models are usually based on a restricted number of factors and thus do not capture the multi-layered architecture of signaling during EMT (Hong et al., 2015; Zhang et al., 2014). To date, no EMT-focused studies have simultaneously measured metabolite and gene expression changes at different functional levels (e.g., mRNA, total protein, nucleus, secretome, etc.).

Consequentially, several aspects of EMT remain unclear. This includes dependencies between molecular layers, secreted molecules, and specific signatures at various stages of EMT, kinetics and scope of metabolic reprogramming, dynamics of subcellular protein localizations and ligand-receptor mediated intercellular crosstalk. To bridge these gaps, we employed multiple high-throughput platforms including microarray, scRNAseq and precision mass spectrometry (MS) to quantify molecules spanning 12 distinct layers of biological information. Our ability to integrate this information allowed us to define signatures of E/M states and identify molecular regulators of key transition points.

RESULTS

A comprehensive resource on TGFβ-induced EMT

The human mammary epithelial cell line MCF10A is widely used to study TGFβ (transforming growth factor β) induced EMT. To generate temporal expression maps of evolving EMT landscape, cells were treated with TGFβ (TGF-β1; 10 ng/mL) over 12 days (0, 4 hrs, 1–6, 8 & 12 days), spanning multiple 'omics' layers and employing complementary technologies (**Fig. 1A-B**, **Fig. S1A-C**). After stringent quality control (see **STAR Methods**), we report nanoLC-MS/MS-based quantifications (**Fig. 1C**, **Table S1**) of 6,540 whole cell (*WC*), 4,198 nuclear (*Nuc*), 2,223 plasma membrane (*Mem*), 1,209 extracellular vesicle (*EV*) and 1,133 secreted (*Sec*) proteins. Using a serial enrichment workflow (see **STAR Methods**) we also quantified the total phosphoproteome (*Phos*; 8,741 high-confidence sites on 2,254 proteins; including 6,975 Ser, 962 Thr and 140 Tyr residues), N-glycoproteome (*Glyco*; 549 proteins), acetylome (*Acet*; 349 sites on 165 proteins) and peptidome (*Pep*; 547 peptides from 202 proteins). For proteomics, samples for ten time point were multiplexed using isobaric tandem mass tags (TMT-10), enabling higher throughput and robust comparisons. In addition to proteins, we tracked cellular metabolism in the same samples by nanoLC-MS/MS-based untargeted metabolomics, quantifying 4,259 HMDB-indexed endogenous small molecules (*Metabol*). Furthermore, we measured 23,787 gene transcripts (mRNA) and 2,578 microRNAs (miRNA) using microarrays. To assess cellular heterogeneity, we employed scRNAseq to quantify transcriptomes of 1,913 individual cells (>200 cells per time point) undergoing EMT. In total, this study provides temporal quantifications of >60,000 proteins, phosphosites, mRNAs, miRNAs, and metabolites combined, in addition to 9,785 mRNAs in scRNAseq dataset (**Fig. 1C**).

Subcellular enrichments were performed using previously established MS-compatible protocols (see **STAR Methods**), yielding high purity as determined through keyword matching against a cellular compartment annotation database (**Fig. S1D**). Quantitative reproducibility across the 3 biological replicates was excellent (**Fig. S1E**). The expression profiles in **Fig. 1D** provide a snapshot of concurrent changes of a given gene over various layers during EMT. We reproduced expected expression behavior for many established markers of EMT, including an increase of M markers VIM, CDH2 and concomitant decrease of E markers SCRIB, MUC1.

Using strict criteria for differential expression (Benjamini-Hochberg adj. *p-value* < 0.05; $r^2 \geq 0.6$ & $|\log2FC| \geq 1$) we identified >10,000 significantly regulated molecules (**Table S2**). We found that molecular abundances were highly variable across layers and time points (**Fig. S1F**) and all layers contributed significantly to the overall variation in the system (**Fig. 1E**). While each layer showed substantive alterations, the magnitudes (**Fig. S1G**), response profiles (**Fig. 1F**) and fraction of differentially expressed molecules (**Fig. 1G**) of each omic data set during the time course varied significantly. These findings provide direct evidence for global reorganization of cell physiology during EMT. For example, *Phos* and *Sec* showed the highest fractional change (36% & 40%, respectively) (**Fig. 1G**), suggesting extensive intra- and extra-cellular signaling during EMT (Scheel et al., 2011). As such, this study is the largest experimental description of EMT till date and adds new

depth to our current understanding of TGFβ signaling and EMT (**Fig. 1H, I**).

Integrative multi-tiered topology of EMT reveals key transition points and identifies molecular drivers

Although E→M progression is considered a continuum, the existence of E, hybrid E/M, and M states have been reported for MCF10A cells (Zhang et al., 2014), and cancer tissues (Liu et al., 2019; Pastushenko et al., 2018). Using a phylogenetic clustering approach (Hughes and Friedman, 2009) we estimated 'distances' between time steps to understand the transition kinetics (**Fig. 2A**). We observed that up to 24 hours cells maintained their parental E type, while day 2 marked a swift exit from E, and entry into E/M which continued through Day 5, after which cells gradually entered the M state. Cells in day 2 to 5 can be further sub-divided into E/M–1 (Day 2/3, late E) and E/M–2 (Day 4/5, early M) states. These cellular reconfigurations agreed with principal component analysis of individual layers, such as *Mem*, *Phos* and *WC* (**Fig. S2A**).

Our observations suggest a distinct and complementary role for each molecular layer in shaping the transition (**Fig 2B**, **Fig 1E-G**, **Fig S1F, G**). Although, the topology was generally correlated (**Fig. 2C**), pairwise coefficients of determination (adj. R^2) revealed an unexpectedly low concordance between total proteins and other proteomic layers (mean R^2 ranging from 0.015 for *Acet* to 0.299 for *Glyco*) (**Fig. 2D, Upper panel**). The discordance was even stronger between mRNA and various proteomic layers (mean R^2 ranging from 0.011 for *Pep* to just 0.109 for *WC*) (**Fig. 2D, Lower panel**), which increased further with EMT progression. Collectively, these observations illustrate that at a systems level mRNA quantity is a poor proxy of protein abundance. Even total protein quantity is an unreliable predictor of post-translational modifications or subcellular trafficking, which ultimately determines signaling output.

Next, we modeled the regulatory patterns of molecules using a 3-step computational workflow. First, we used a regression strategy for time-course measurements (Conesa et al., 2006) to remove residual noise (time dimension) and non-reliable (replicates) components. Second, an unsupervised machine learning approach (self-organizing maps, SOMs) (Wirth et al., 2012) was applied on the retained molecules to generate time-point specific SOM portraits (**Fig. 2E, Fig. S2B-D**, see **STAR Methods** for details). SOMs are a powerful integration tool for diverse global datasets to extract underlying patterns of co-regulation (Tamayo et al., 1999). Third, we performed pathway enrichments of these SOMs to elucidate the overarching functional themes at each time-step of EMT (**Fig. 2F**).

SOMs traced the temporal unfolding of the transition and provided molecular fingerprints of each time-step. Molecules ranking high (top 1% i.e., rank ≤ 250 & log2FC ≥ 1) with SOMs for control to day 1 (430 unique molecules) primarily included proteins characteristic of an E state (**Fig. 2E, Table S3**), such as, ACTG1 (*Mem*; establishes cell junctions and shape) and EPHB2 (*Glyco*; regulates angiogenesis, contact dependent adhesion and migration; tumor suppressor). SOMs for days 6–12 (252 unique molecules) contained known M markers, e.g., CALD1, CDH2, FLNA, FN1, FSTL1, LGALS1,

168 NT5E, TAGLN, TPM1, TPM2, TPM4 and VIM. This group also included molecules with established
169 roles in cancer and EMT, including miR-5189 (*miR*; targets ARF6 which internalizes CDH1), CALR
170 (*Acet*; Lys 62; calcium homeostasis, promotes metastasis, imparts resistance to anoikis), ALCAM
171 (*Nuc*; prognostic marker in multiple cancers linked to nuclear translocation of β-catenin and
172 stemness), ARHGAP33 (*Sec*; regulates intracellular trafficking), RAPGEF5 (*Sec*; promotes nuclear
173 translocation of β-catenin) and SOCS3 (*Phos*; Thr 3/13; E3 ligase, E3 ligase inhibiting TGFβ signaling).
174 As suggested in **Fig 2A**, the first major shift, E→E/M, occurred at day 2 and was likely driven by
175 molecules peaking at its corresponding SOM (95 molecules) such as miR-675-5p/H19 (*miR*; induces
176 HIF1α, SNAIL activity), LTBP1 (*Sec*; master regulator of integrin-dependent TGFβ activation) and
177 CD44 (*Sec*; signal transduction). Notably, many of the molecules identified in the SOM analysis, to our
178 knowledge, have not been previously linked to TGFβ signaling or EMT, presumably because they do
179 not show clear changes in *mRNA* or *WC* but in 'other' molecular layers, such as *EV* or *Sec* (**Fig. S2E**).
180 This contrasts with most MSigDB hallmarks of EMT for which we captured clear transcriptional
181 profiles (**Fig. S2F**).

182 Gene-set enrichment analysis using active subnetworks which yields more robust inferences than
183 traditional approaches (Ulgen et al., 2019), identified 237 significant pathways (**Fig. 2F**, **Table S3**),
184 discretized across sequential steps of EMT. For example, 'Beta oxidation of hexanoyl-CoA to butanoyl-
185 CoA' declined as cells leave E and enter E/M, indicating reprogramming of mitochondrial fatty acid
186 β-oxidation, consistent with a metastatic phenotype (Ma et al., 2018). Conversely, 'RHO GTPases
187 mediated activation of ROCKs/PAKs/IQGAPs' increased as cells leave E/M and enter M, suggestive of
188 their key role at this stage of EMT (Ungefroren et al., 2018). The E/M specifically were associated
189 with migration-associated pathways such as 'anchoring fibril formation', 'ECM proteoglycans' and
190 'laminin interactions', consistent with their shared property with CTCs.

191 Overall, we catalogued complex kinetics of thousands of molecules spanning multiple molecular
192 layers during EMT. Importantly, we identify critical transition points during EMT and predict
193 signatures specific to each stage, e.g., E/M, with potential clinical value.

194

195 Metabolomics reveals kinetics and predicts novel enzyme-metabolite associations

196 TGFβ regulates Warburg effect in cancer cells, but may also regulate other metabolic pathways with
197 implications for cancer management (Hua et al., 2019). Active subnetwork analysis of *WC* and *Phos*
198 datasets identified 13 enriched KEGG metabolic pathways during TGFβ-induced EMT (**Fig. S3A**).
199 Notably, significant enrichment (*p–value* ≤ 0.05) for any pathway was only observed after day 2 and
200 included processes such as steroid hormone biosynthesis (SHB), sphingolipid metabolism and (SLM)
201 glycosaminoglycan degradation (GMGD). To evaluate these gene-centric inferences of metabolic
202 phenotypes, we directly profiled intra-cellular small molecules by applying an optimized untargeted
203 metabolomics workflow to the same set of samples. Using stringent criteria (see **STAR Methods**), we
204 quantified >4,000 putative HMDB-compounds covering a wide range of chemical classes (**Fig. 3A**).

205 Using phylogenetic clustering (**Fig. 3B**) and SOM analysis (**Fig. 3C**) driven solely by the *Metabol*
206 dataset, we observed the E→E/M transition as early as 4 hours, followed by another transition after
207 day 1. This indicates rapid modulation of cellular metabolism by TGFβ, preceding changes in most
208 other layers. The E/M→M transition occurred around day 5, in line with the integrative analysis.

209 To glean further insights, we performed integrative network analysis of metabolite SOMs with
210 differential molecules in *WC* and *Phos* using MetaboAnalyst (Chong et al., 2019) (**Fig. 3D**). This
211 analysis reiterated several enriched pathways predicted with protein expression alone, e.g., SHB,
212 SLM, GMGD, glycerophospholipid metabolism (GPLM) and lysine degradation (LD) (**Fig. S3A**).
213 However, integration of metabolite and protein data within the framework of metabolite SOMs
214 revealed pathway activities representative of key transition steps of EMT driven primarily by
215 corresponding metabolite signatures (**Fig. S3B-D**). Indeed, we observed that arachidonic acid
216 metabolism (AAM), GPLM and LD pathways were activated within 4 hours of TGFβ stimulation,
217 which was not captured by gene-set analysis. Consistent with observations in **Fig 2F**, processes such
218 as fatty acid metabolism, SHB and SLM appear after day 2, as cells prepare for a metastatic phenotype
219 (Koundouros and Poulogiannis, 2020).

220 Pairwise-correlation based integration of metabolite profiles with proteomics measurements from
221 the same samples could enable mechanistic predictions and aid discovery of novel players. To
222 explore this, we chose AAM as an example. Arachidonic acid is an omega-6 fatty acid stored as
223 membrane phosphoglycerolipid. Its cytosolic release enables stoichiometric chain reactions and
224 results in >100 functionally diverse compounds (Hanna and Hafez, 2018) impacting processes such
225 as redox state, proliferation, apoptosis and chemotaxis (Tallima and El Ridi, 2018). We computed
226 Pearson's correlations between abundance of KEGG-annotated enzymes, in *WC* and *Phos*, and
227 metabolites of AAM pathway, in *Metabol*, quantified at SOM for 4 hours to day 1 (**Fig. 3E, F**). Overall,
228 we found that metabolites mapping to AAM either rapidly increased and then stabilized (Cytochrome
229 P450, CYP450, branch) or showed a delayed but consistent increase over the time course
230 (Cyclooxygenase, COX, and Lipoxygenase, LOX, branches) (**Fig. 3G**), suggesting fine-tuned regulation
231 of the different branches. Encouragingly, our enzyme-metabolite association map identified
232 PLA2G4A, the rate-limiting phospholipase of AAM pathway (Hanna and Hafez, 2018), among the top
233 candidates (**Fig. 3F**). Interestingly, correlation and expression profiles of PLA2G15, another
234 phospholipase, (**Fig. 3E-G**) indicated a potential enzyme-mediated switch from CYP450 to COX/LOX
235 branches during E→E/M.

236 Overall, these observations reveal the kinetics of metabolic reprogramming during TGFβ induced
237 EMT. We found metabolites and protein signatures coordinating processes such as AAM, GPLM and
238 LD during key stages of the transition. We also demonstrate how our enzyme-metabolite correlation
239 map could be used as a resource to predict novel enzymes for observed metabolic changes.

240

scRNAseq analysis reveals heterogeneous responses to TGFβ and novel transcriptional regulators of EMT

scRNAseq studies in murine epithelial Py2T cells treated with TGFβ (Krishnaswamy et al., 2018), MCF10A cells undergoing confluence-dependent EMT (McFaline-Figueroa et al., 2019) and LPS-induced EMT in alveolar epithelial cells (Riemondy et al., 2019), provided valuable insights into EMT. However, a temporal analysis of TGFβ-induced EMT to understand the transition states has not been reported.

After quality control, we retained 1,913 single cells with a combined depth of 9,785 genes (**Fig. S4A, Table S1**). As anticipated, many of the top expressing genes (TGFB1, TPT1, KRT6A, TMSB10, MT2A) are key players in EMT (**Fig. S4B**). Interestingly, similar to many primary human tumors (Puram et al., 2018), we did not observe an explicit loss of several classical E markers at the transcript level (**Fig. 4A, Fig. S4C**), suggesting post-transcriptional regulation, a strategy which could be energetically economical for tumor cells (Lambert et al., 2017).

To understand the stages of cell differentiation, we took advantage of the multiple time points in our dataset (as opposed to a 'pseudo-time'), and identified 20 cell clusters in 3 disjoint partitions, using Monocle3 (**Fig. 4B, Fig. S4D**). Partition P2 (12 clusters) represents the primary EMT axis while P1/P3 predominantly expressed genes related to cell cycle (**Fig. S4E**) and were ignored for further analysis. We observed that C3 responded strongly to TGFβ (**Fig. 4C**), C4/6 resisted EMT, C5/C8 are the 'transition' states and C13/14 represented terminal M cells (in terms of hallmark M markers; **Fig. 4C, right panel**). Examining clusters C9/18/19 which were composed of cells from nearly all time points, suggests presence of stable M-type cells in MCF10A populations and appears to be at transcriptional impasse for TGFβ signaling. Notably, using scRNAseq, we could observe an E→E/M transition, but the E/M→M transition, as revealed by integrative analysis, was not clear.

To explore the underlying gene expression program, we used hierarchical clustering to group the individual clusters into 6 subtypes (**Fig. 4C**) and employed SCENIC (Aibar et al., 2017) to infer TFs and GRNs underlying these subtypes (**Fig. D-F; Table S5**). For each subtype, we identified several unique (**Fig. 4E**) or highly active TFs (**Fig. 4F**), including both established and novel players. Several TFs implicated in EMT (TWIST2, FOXK2, ZEB1, ID2, MSX1, ING4) were over-represented in S4-S6, which corresponds to later stages of EMT. In contrast, direct evidence of mechanistic links of TFs enriched in early stages of EMT (i.e., S3, S4) are lacking, indicating gaps in current EMT models. Using human TF–binding arrays (see **STAR Methods, Fig. 4G**) we confirmed elevated activity of three S3 TFs, GLIS2, SP1 and ZNF266 upon TGFβ induction (**Fig. 4H**). In addition to providing experimental evidence to our predictions, the TF-binding array also revealed several other TFs potentially playing important roles at the early stages of EMT (**Fig. 4I**).

Overall, we provide a high-resolution temporal map of gene expression programs of individual cells as they respond to TGFβ signaling and undergo EMT. More generally, our data suggests that most transcriptional changes occur at early time points (also **Fig. 2D, Lower panel**), followed by further adaptations driven predominantly by post-transcriptional mechanisms.

Spatial regulation of proteins and inter-cellular communication during EMT

Regulation of protein distribution is a crucial signaling mechanism (Ferrell, 1998), but remains insufficiently understood in EMT. The average Pearson's correlation between proteins quantified in multiple cellular compartments (CCs) ranged between r = 0.12 to 0.58 indicating fine-tuned regulation of protein distributions (**Fig. 5A**). We found 3,965 proteins localizing to ≥2 CCs (**Fig. S5A**), which we categorized into 2 classes as follows: Class I proteins (1,424) displayed a correlated trend ($r \geq 0.4$) consistently across all CC pairs suggesting regulation primarily at or before the translation step (**Fig. 5B, C; Table S5**). Class II proteins (1,205) displayed anti-correlated trend ($r \leq -0.4$) between any two CCs, implying active post-translational control of their asymmetric distributions (**Fig. 5D, E; Table S5**).

The Bromodomain and ExtraTerminal (BET) cofactors, BRD2 and BRD4, were identified as Class II proteins (**Fig. 5F**). Using TF-binding arrays, we verified enhanced global recruitment of BRD4, but not two other cofactors, p300 and LSD1, (**Fig. 5G**) indicating its specific role during EMT. Indeed, treatment with a selective BET inhibitor JQ-1 suppressed EMT (**Fig. 5H**). Another notable Class II protein was SCRIB (**Fig. 5I**), which regulates apical-basal polarity and directional migration by acting as a molecular scaffold through protein-protein interactions (PPIs) (Bonello and Peifer, 2019). Using an *in* vivo proximity ligation (BioID) screen of SCRIB ((**Fig. S5B**, see **STAR Methods**), we identified multiple novel interactors (**Table S6**) of which many have known roles in EMT (**Fig. 5J**). Using immunoprecipitation, we verified interactions of SCRIB with SNAP23 and ARHGEF7 (**Fig. 5K**).

Subtypes within a cell population can differ in their capacity to send and receive signals, with implications for metastasis and drug resistance (Kim et al., 2018; Tabassum and Polyak, 2015). To map the inter-cellular communication between subgroups of cells during TGFβ-induced EMT, we integrated proteomics and scRNAseq data to perform a systems-wide survey of ligand-receptor (L-R) pair mediated crosstalk (**Fig. 5L**). First, using a database of >2,500 curated binary L-R interactions (Ramilowski et al., 2015), we searched for pairs of L and R in our *Sec* and *Mem/Glyco* datasets, respectively, assuming that co-directional expression changes in L and/or R of a pair (FDR adj. *p-value* < 0.05 and combined L-R |log2FC| ≥1) can indicate biological role. Currently, at least two L-R pairs are implicated in TGFβ-induced EMT (Heldin et al., 2012). Our analysis detected 67 upregulated and 12 downregulated L-R pairs at any given time point following TGFβ treatment (**Fig. 5M, Table S7**). Notably, none of these pairs have been directly implicated in TGFβ signaling or EMT, although individually many of the identified L or R occur frequently in the context of EMT and/or cancer. For instance, LAMC2 with its 7 receptors (CD151, COL17A1, ITGA2, ITGA3, ITGA6, ITGB1, ITGB4) exhibit significant alteration during EMT. LAMC2 is overexpressed in cancers (Garg et al., 2014) and its silencing can reverse EMT (Pei et al., 2019). The cognate receptors, CD151, ITGA3, ITGA6 and ITGB1 synergize with TGFβ signaling to promote metastatic behavior (Pellinen et al., 2018; Sadej et al., 2010; Shirakihara et al., 2013; Zhang et al., 2017).

Next, by systematically comparing the expression patterns of L & R (identified above) among the 16

317 clusters (identified in our scRNAseq dataset), we obtained cell-cell communication networks (sender
318 → receiver) (**Fig. 5N, Fig. S5C, Table S7**). For example, C13 cells, which appeared at day 3 and
319 showed highest M genes expression (**Fig. 4C**), produced the receptor CD44 to its cognate ligand
320 MMP7 expressed by C17 (**Fig. S5D**). Together, this suggests that communication between cell
321 subgroups (C17:MMP7 → C13:CD44) may exist during EMT which might have potential ramifications
322 for tumor growth. Interestingly, our analysis suggests a global switch in cell surface proximal
323 signaling cascades at day 2, corresponding to E→E/M transition, and likely modulating processes
324 characteristic of E/M cells, e.g., migration (e.g., FN1–ITGB6) and stemness (e.g., TIMP2–ITGA3).

325 As independent corroboration, several identified L-R pairs showed strong correlation (**Fig. 5O**) in
326 human breast invasive carcinoma samples (Cancer Genome Atlas Network, 2012; Cerami et al.,
327 2012). Notably, a slightly stronger correlation between the L–R pairs was observed with CPTAC
328 proteomics data than with TCGA mRNA datasets.

329 Our study provides a comprehensive analysis of TGFβ-triggered subcellular trafficking as cells
330 undergo EMT. Such translocations, potentially driven by differential PPI, could mediate the tight
331 coordination between functional modules (e.g., SCRIB complex) and EMT phenotypes such as
332 cytoskeletal rearrangement. We also uncovered novel cell-cell communication pathways via L-R
333 interactions in driving EMT, representing an untapped clinical opportunity.

334

335 Modeling phosphoproteome dynamics during EMT reveals kinase susceptibilities

336 Phosphoregulatory mechanisms are a key aspect of TGFβ signaling and EMT. We confidently
337 quantified 8,741 phosphosites (p-sites; 6,975 Ser, 962 Thr and 140 Tyr residues) (**Fig. S6A-C**) over a
338 dynamic range of 10^6 orders of magnitude (**Fig. S6D**), and phospho–STY frequencies (**Fig. S6E**) in
339 line with previous reports (D'Souza et al., 2014) mapping to 2,254 proteins (**Fig. S6F**). Of all p-sites,
340 3,138 (35.8%) were differentially regulated in at least one time point (**Fig. S6G**). At protein level,
341 different patterns of regulation were noted; some proteins, such as DEK, VIM and MISP, were
342 regulated at ~90% of detected sites, some proteins, such as CAV1, CAMK2 and GOLGA1, showed a
343 ~50% mixture of regulated and unregulated sites, while others such as AHNAK, PML and BCLAF1
344 showed ~2% differential sites (**Fig. 6A**). Interestingly, the fraction of regulated p-sites in several
345 proteins, e.g., VIM, increased with EMT progression (**Fig. 6B**).

346 We observed that in ~50%, p-sites dynamics were not explained ($r \leq 0.4$) by a corresponding change
347 at the protein level (**Fig. 6C, D**). Interestingly, for ~26%, a directionally opposite change between
348 phosphorylation and the corresponding protein abundance was noted ($r \leq -0.1$), suggesting effects
349 on protein stability. Phospho-regulated proteins were enriched for 'nucleus', 'cytoskeleton' and 'focal
350 adhesion' annotations (**Fig. 6E**) reflecting the importance of CC remodeling during EMT.

351 We also computed correlations between nuclear localization profiles (*Nuc*) and phosphorylation
352 kinetics (*Phos*) of individual proteins (**Fig. 6F, G**). For instance, phosphorylation of MICAL3 at T684
353 and S685 regulates CSCs by promoting symmetric division (Tominaga et al., 2019). The pattern of

354 phosphorylation of MICAL3 at residues T684, S685 and S687 (**Fig. 6D,** MICAL3) which are located at
355 the consensus NLS motif suggests a role in regulating nuclear translocation of MICAL3 at E→E/M
356 transition. Indeed, the bipartite NLS motif of MICAL3 interacts with Importin-α and the p-sites T684,
357 S685, S687 are directly adjacent to the binding interface (**Fig. 6H**).

358 To analyze stage-specific kinase activities we generated a ternary model which distinguishes active
359 kinases into 3 broad stages (i.e., E, E/M, and M) of EMT (**Fig. 6I**). An example that illustrates the utility
360 of this model are AKT isoforms that have distinct and opposing roles during cancer development
361 (Hinz and Jücker, 2019). We predict AKT1 is strongly associated with the E-stage, which is consistent
362 with its role in maintaining the E phenotype (Li et al., 2016). In fact, depletion of AKT1 in MCF10A
363 cells promoted TGFβ-induced E→E/M transition (Iliopoulos et al., 2009). Our model further predicts
364 key roles for AKT2 and AKT3 at E/M→M transition. Indeed, AKT2 and AKT3 were associated with
365 tumor invasiveness, stemness and sensitivity to drug treatment (Chin et al., 2014), key characteristics
366 of the E/M populations (Dongre and Weinberg, 2019). Among several other kinases (**Fig. 6J, Fig.**
367 **S6H**), our ternary model predicted key roles for PRKCA and AURKB at the junction of E→E/M and
368 E/M→M transitions. PRKCA is reportedly a hub and therapeutic target for EMT-induced breast CSCs
369 (Tam et al., 2013). Similarly, inhibition of AURKB was found to reverse EMT and reduce breast cancer
370 metastasis *in vivo* (Zhang et al., 2020).

371 Overall, we reveal the rich intricacies of the phosphoregulome during EMT, identified functional p-
372 sites, predict novel kinase susceptibilities, and provide a mechanistic framework to enhance
373 understanding of the signaling mechanisms during EMT.

374

375 **Integrative systems causal model of EMT identifies mechanistic vulnerabilities**

376 Systems biology approaches that combine multiple molecular types (proteins, mRNAs, miRNAs,
377 metabolites) into a framework of established knowledge allow for a rich assessment of a biological
378 context (Hawe et al., 2019). Using experimentally validated functional priors (compiled from
379 ENCODE, PhosphoSitePlus, SignaLink 2.0, SIGNOR 2.0, HINT, miRTarBase and MetaBridge), we
380 combined causal inference and PCSF (Prize Collecting Steiner Forest) (Akhmedov et al., 2017) to
381 construct hierarchical mechanistic models of the EMT program (**Fig. 7A**, see **STAR Methods**). The
382 final 'EMT network' comprised of 3,255 edges connecting 2,217 molecules, including 723
383 kinase/phosphatase–substrate, 1,407 TF–target, 746 miRNA–target and 31 metabolite–gene
384 interactions.

385 One of the potential applications of the EMT network is to discover signaling paths from TGFBR1/2
386 to any gene(s) of interest within the network. As a demonstration, we queried several EMT-
387 associated genes (FN1, MMP7, CD44, SCRIB, TWISTNB, ZEB1, SNAI2) and recovered previously
388 known and unknown paths to them putatively active at multiple stages of EMT (**Fig. S7A**). Next, to
389 identify key factors driving EMT, we performed 'controllability' analysis (Vinayagam et al., 2016) to
390 identify controllers (nodes) exerting a significant influence on EMT network topology. Not

391 surprisingly, a few of them are established key regulators of metastasis (**Fig. 7B**). Unlike controllers,
392 however, the non-controller nodes were poorly represented in EMT literature (**Fig. 7C**), again
393 highlighting gaps, and potentially identifying new regulatory processes. Survival analysis against a
394 large publicly available dataset of primary breast cancers with long-term patient outcomes (Cancer
395 Genome Atlas Network, 2012) showed a significant association between tumors with altered
396 expression of these controllers and shortened overall survival (**Fig. 7D**).

397 We queried the EMT network to identify signaling contexts in which these controllers are active at
398 various key stages of EMT, which could also provide clues into mechanistic vulnerabilities (**Fig. 7E**).
399 As cells are stimulated with TGFβ, the TFs SMAD2 and SMAD3 are activated, as expected. Another
400 early responder was RHO GTPase RAC1, an effector of both KRAS (Wu et al., 2014) and TGFβ signaling
401 (Ungefroren et al., 2018), suggesting potential crosstalk. The downstream effector of RAC1, MAPK14
402 (p38 MAPK), was also regulated early in EMT, suggesting cooperation between RAC1 and MAPK
403 pathways (Santibáñez et al., 2010). Our model suggests SMAD3 regulates two other TF hubs, CEBPB
404 (CCAAT/enhancer-binding protein β) and FOXA1. Loss of CEBPB reportedly switches TGFβ signaling
405 from growth-inhibiting to EMT-inducing (Johansson et al., 2013), while FOXA1 is reportedly a key TF
406 during EMT (Wang et al., 2013). We observed that STAT3 is suppressed at later stages of EMT. A
407 recent study in KRAS-driven lung and pancreatic cancer found that STAT3 is required for maintaining
408 the E state and is lost during acquisition of M phenotypes (D'Amico et al., 2018).

409 The EMT network directly predicts novel avenues for blocking EMT. To assess this, we performed a
410 morphometry-based screening where we treated MCF10A cells with TGFβ in combination with drugs
411 which were predicted to inhibit several of the controllers active at E→E/M transition (**Fig. 7F,** see
412 **STAR Methods**). Our analysis using a custom-built (Ochs et al., 2019) and publicly accessible image
413 analysis software GENIMASEG (**Fig. 7F**) showed significant efficacy of LB100+Barasertib,
414 LB100+PP1 and Sonidegib+Autocamtide in reverting the elongated phenotype of EMT-induced cells
415 (**Fig. 7G**), thus providing direct experimental evidence to our predictions. Using a biomimetic 3D
416 mammary duct-on-a-chip platform (Kutys et al., 2020), we further observed that combinatorically
417 inhibiting SMO and CAMK-II (Sonidegib+Autocamtide) inhibits invasion driven by the PI3K variant,
418 PIK3Cα^{H1047R}, which is associated with chemo-refractoriness in a subset of triple negative BrCa
419 patients (Janku et al., 2013).

420 Overall, our EMT network recapitulates known signaling pathways, uncovers novel routes of
421 information flow to known regulators of EMT, identifies new signaling players and pathways, makes
422 substantial and provocative novel predictions and reveals cohesive time-resolved regulatory
423 patterns and mechanistic links between both controllers and non-controllers.

424

425 DISCUSSION

426 EMT and cancer are *emergent systems* (Sigston and Williams, 2017) wherein progression through
427 various stages is regulated by intricate networks of intra- and extra-cellular signaling within and

428 between cells. The key to understanding such complex biological phenomena are establishing
429 experimental workflows that integrate multiple tiers of biological information (Karczewski and
430 Snyder, 2018).

431 Discussions on EMT are often guided by the Waddington metaphor of a ball (=cell) rolling over a
432 phenotypic landscape, which is dynamically shaped by multiple parameters: topologies of signaling
433 networks, molecular stochasticity, extraneous cooperating and opposing forces (e.g., EMT inducing
434 and/or inhibitory ligands, interaction with other cells) (Li and Balazsi, 2018). By integrating several
435 molecular layers, SOMs and 'neighbor joining' approaches revealed the kinetics of cell-fate
436 transitions and major phenotypic switch points driven by TGFβ. Several studies have indicated
437 molecular and phenotypic granularity in EMT continuum and suggested existence of discrete
438 metastable E/M (Sha et al., 2019). Many current EMT markers are biased toward the later stages of
439 EMT, when the process is approaching completion (Song et al., 2019). Consequently, the molecular
440 nature of E/M is still poorly understood. Our time-course integrative SOM allowed us to trace the
441 temporal unfolding and uncover the molecular nature of the E→M transition.

442 While previous omics studies have measured either one or two molecular layers to describe EMT,
443 our multi-tiered datasets enabled the discovery of several new aspects of EMT which were not
444 captured by previous approaches. For example, the correlation between *mRNA* and proteins were
445 weak. Strikingly, correlations between the various *proteomics layers* were also found to be quite poor,
446 indicating that systems behavior cannot readily be extrapolated by any single layer (e.g., mRNA or
447 total proteome), but instead needs an integrated analysis of several molecular layers. We show that
448 TGFβ-induced EMT is only partially driven by transcription, where several E genes are repressed
449 only post-transcriptionally, while transcripts of M genes are upregulated but mostly during earlier
450 time points. At later stages, post-translational mechanisms become more prominent in driving the
451 process, suggesting that the regulatory control of EMT may be more flexible than previously
452 appreciated. Similarly, our results also predict the mechanistic importance of protein subcellular
453 localization during EMT. A comparison of proteins detected in *EV*, *Sec*, *Glyco*, *Mem* and *Nuc* indicated
454 extensive regulation of protein localizations. Further, previous studies on EMT have largely focused
455 on cell-autonomous signaling, whereas multiple inter-cellular signaling mechanisms are evident
456 from our integrative analysis. Indeed, we found both *EV* and *Sec* to be extensively regulated during
457 EMT. Once considered as cellular 'garbage bins', their active participation in signaling and crosstalk
458 is increasingly recognized (H. Rashed et al., 2017). Our results demonstrating limited qualitative
459 overlap between *EV* and *Sec* hint at a potentially overlooked mechanistic distinction and provides
460 opportunities for new biological insights. We utilized our *Mem*, *Glyco* and *Sec* datasets to provide a
461 repertoire of 79 putative new L-R pairs with potential roles during EMT, which should be validated
462 in future studies. By combining these results with the scRNAseq profiles, we were able to define an
463 extensive network of inter-cellular communications.

464 In conclusion, we have established a comprehensive multi-tiered molecular landscape of TGFβ-
465 induced EMT. This study aims to provide a valuable resource which is accessible through an

466 interactive website (https://www.bu.edu/dbin/cnsb/emtapp/) (**Fig. S7**) and will strongly
467 complement hypothesis-driven research with direct implications for epithelial cancers.

468 # REFERENCES

469 Aibar, S., González-Blas, C.B., Moerman, T., Huynh-Thu, V.A., Imrichova, H., Hulselmans, G., Rambow,
470 F., Marine, J.-C., Geurts, P., Aerts, J., et al. (2017). SCENIC: Single-cell regulatory network inference
471 and clustering. Nat. Methods *14*, 1083–1086.

472 Akhmedov, M., Kedaigle, A., Chong, R.E., Montemanni, R., Bertoni, F., Fraenkel, E., and Kwee, I.
473 (2017). PCSF: An R-package for network-based interpretation of high-throughput data. PLOS
474 Comput. Biol. *13*, e1005694.

475 Bonello, T.T., and Peifer, M. (2019). Scribble: A master scaffold in polarity, adhesion,
476 synaptogenesis, and proliferation. J. Cell Biol. *218*, 742–756.

477 Cancer Genome Atlas Network (2012). Comprehensive molecular portraits of human breast
478 tumours. Nature *490*, 61–70.

479 Cerami, E., Gao, J., Dogrusoz, U., Gross, B.E., Sumer, S.O., Aksoy, B.A., Jacobsen, A., Byrne, C.J., Heuer,
480 M.L., Larsson, E., et al. (2012). The cBio Cancer Genomics Portal: An Open Platform for Exploring
481 Multidimensional Cancer Genomics Data: Figure 1. Cancer Discov. *2*, 401–404.

482 Chin, Y.R., Yoshida, T., Marusyk, A., Beck, A.H., Polyak, K., and Toker, A. (2014). Targeting Akt3
483 Signaling in Triple-Negative Breast Cancer. Cancer Res. *74*, 964–973.

484 Chong, J., Wishart, D.S., and Xia, J. (2019). Using MetaboAnalyst 4.0 for Comprehensive and
485 Integrative Metabolomics Data Analysis. Curr. Protoc. Bioinforma. *68*, e86.

486 Conesa, A., Nueda, M.J., Ferrer, A., and Talón, M. (2006). maSigPro: a method to identify significantly
487 differential expression profiles in time-course microarray experiments. Bioinforma. Oxf. Engl. *22*,
488 1096–1102.

489 D'Amico, S., Shi, J., Martin, B.L., Crawford, H.C., Petrenko, O., and Reich, N.C. (2018). STAT3 is a
490 master regulator of epithelial identity and KRAS-driven tumorigenesis. Genes Dev. *32*, 1175–1187.

491 Dongre, A., and Weinberg, R.A. (2019). New insights into the mechanisms of epithelial–
492 mesenchymal transition and implications for cancer. Nat. Rev. Mol. Cell Biol. *20*, 69–84.

493 D'Souza, R.C.J., Knittle, A.M., Nagaraj, N., Dinther, M. van, Choudhary, C., Dijke, P. ten, Mann, M., and
494 Sharma, K. (2014). Time-resolved dissection of early phosphoproteome and ensuing proteome
495 changes in response to TGF-β. Sci. Signal. *7*, rs5–rs5.

496 Ferrell, J.E. (1998). How regulated protein translocation can produce switch-like responses. Trends
497 Biochem. Sci. *23*, 461–465.

498 Garg, M., Braunstein, G., and Koeffler, H.P. (2014). LAMC2 as a therapeutic target for cancers. Expert
499 Opin. Ther. Targets *18*, 979–982.

500 H. Rashed, M., Bayraktar, E., K. Helal, G., Abd-Ellah, M.F., Amero, P., Chavez-Reyes, A., and Rodriguez-
501 Aguayo, C. (2017). Exosomes: From Garbage Bins to Promising Therapeutic Targets. Int. J. Mol. Sci.
502 *18*.

503 Hanna, V.S., and Hafez, E.A.A. (2018). Synopsis of arachidonic acid metabolism: A review. J. Adv. Res.
504 *11*, 23–32.

505 Hawe, J.S., Theis, F.J., and Heinig, M. (2019). Inferring Interaction Networks From Multi-Omics Data.
506 Front. Genet. *10*.

507 Heldin, C.-H., Vanlandewijck, M., and Moustakas, A. (2012). Regulation of EMT by TGFβ in cancer.
508 FEBS Lett. *586*, 1959–1970.

509 Hinz, N., and Jücker, M. (2019). Distinct functions of AKT isoforms in breast cancer: a
510 comprehensive review. Cell Commun. Signal. CCS *17*.

511 Hong, T., Watanabe, K., Ta, C.H., Villarreal-Ponce, A., Nie, Q., and Dai, X. (2015). An Ovol2-Zeb1
512 Mutual Inhibitory Circuit Governs Bidirectional and Multi-step Transition between Epithelial and
513 Mesenchymal States. PLOS Comput. Biol. *11*, e1004569.

514 Hua, W., ten Dijke, P., Kostidis, S., Giera, M., and Hornsveld, M. (2019). TGFβ-induced metabolic
515 reprogramming during epithelial-to-mesenchymal transition in cancer. Cell. Mol. Life Sci.

516 Hughes, A.L., and Friedman, R. (2009). A phylogenetic approach to gene expression data: evidence
517 for the evolutionary origin of mammalian leukocyte phenotypes. Evol. Dev. *11*, 382–390.

518 Hung, M.-C., and Link, W. (2011). Protein localization in disease and therapy. J. Cell Sci. *124*, 3381–
519 3392.

520 Iliopoulos, D., Polytarchou, C., Hatziapostolou, M., Kottakis, F., Maroulakou, I.G., Struhl, K., and
521 Tsichlis, P.N. (2009). MicroRNAs differentially regulated by Akt isoforms control EMT and stem cell
522 renewal in cancer cells. Sci. Signal. *2*, ra62.

523 Janku, F., Wheler, J.J., Naing, A., Falchook, G.S., Hong, D.S., Stepanek, V.M., Fu, S., Piha-Paul, S.A., Lee,
524 J.J., Luthra, R., et al. (2013). PIK3CA mutation H1047R is associated with response to
525 PI3K/AKT/mTOR signaling pathway inhibitors in early-phase clinical trials. Cancer Res. *73*, 276–
526 284.

527 Johansson, J., Berg, T., Kurzejamska, E., Pang, M.-F., Tabor, V., Jansson, M., Roswall, P., Pietras, K.,
528 Sund, M., Religa, P., et al. (2013). MiR-155-mediated loss of C/EBPβ shifts the TGF-β response from
529 growth inhibition to epithelial-mesenchymal transition, invasion and metastasis in breast cancer.
530 Oncogene *32*, 5614–5624.

531 Karczewski, K.J., and Snyder, M.P. (2018). Integrative omics for health and disease. Nat. Rev. Genet.
532 *19*, 299–310.

533 Kim, E., Kim, J.-Y., Smith, M.A., Haura, E.B., and Anderson, A.R.A. (2018). Cell signaling heterogeneity
534 is modulated by both cell-intrinsic and -extrinsic mechanisms: An integrated approach to
535 understanding targeted therapy. PLoS Biol. *16*.

536 Koundouros, N., and Poulogiannis, G. (2020). Reprogramming of fatty acid metabolism in cancer. Br.
537 J. Cancer *122*, 4–22.

538 Krishnaswamy, S., Zivanovic, N., Sharma, R., Pe'er, D., and Bodenmiller, B. (2018). Learning time-
539 varying information flow from single-cell epithelial to mesenchymal transition data. PLoS ONE *13*.

540 Kutys, M.L., Polacheck, W.J., Welch, M.K., Gagnon, K.A., Koorman, T., Kim, S., Li, L., McClatchey, A.I.,
541 and Chen, C.S. (2020). Uncovering mutation-specific morphogenic phenotypes and paracrine-
542 mediated vessel dysfunction in a biomimetic vascularized mammary duct platform. Nat. Commun.
543 *11*, 3377.

544 Lambert, A.W., Pattabiraman, D.R., and Weinberg, R.A. (2017). Emerging Biological Principles of
545 Metastasis. Cell *168*, 670–691.

546 Li, C., and Balazsi, G. (2018). A landscape view on the interplay between EMT and cancer metastasis.
547 Npj Syst. Biol. Appl. *4*, 1–9.

548 Li, C.-W., Xia, W., Lim, S.-O., Hsu, J.L., Huo, L., Wu, Y., Li, L.-Y., Lai, C.-C., Chang, S.-S., Hsu, Y.-H., et al.
549 (2016). AKT1 Inhibits Epithelial-to-Mesenchymal Transition in Breast Cancer through
550 Phosphorylation-Dependent Twist1 Degradation. Cancer Res. *76*, 1451–1462.

551 Liu, X., Li, J., Cadilha, B.L., Markota, A., Voigt, C., Huang, Z., Lin, P.P., Wang, D.D., Dai, J., Kranz, G., et al.
552 (2019). Epithelial-type systemic breast carcinoma cells with a restricted mesenchymal transition
553 are a major source of metastasis. Sci. Adv. *5*, eaav4275.

554 Liu, Y., Beyer, A., and Aebersold, R. (2016). On the Dependency of Cellular Protein Levels on mRNA
555 Abundance. Cell *165*, 535–550.

556 Ma, Y., Temkin, S.M., Hawkridge, A.M., Guo, C., Wang, W., Wang, X.-Y., and Fang, X. (2018). Fatty acid
557 oxidation: An emerging facet of metabolic transformation in cancer. Cancer Lett. *435*, 92–100.

558 McFaline-Figueroa, J.L., Hill, A.J., Qiu, X., Jackson, D., Shendure, J., and Trapnell, C. (2019). A pooled
559 single-cell genetic screen identifies regulatory checkpoints in the continuum of the epithelial-to-
560 mesenchymal transition. Nat. Genet. *51*, 1389–1398.

561 Nieto, M.A., Huang, R.Y.-J., Jackson, R.A., and Thiery, J.P. (2016). EMT: 2016. Cell *166*, 21–45.

562 Ochs, F., Karemore, G., Miron, E., Brown, J., Sedlackova, H., Rask, M.-B., Lampe, M., Buckle, V.,
563 Schermelleh, L., Lukas, J., et al. (2019). Stabilization of chromatin topology safeguards genome
564 integrity. Nature *574*, 571–574.

565 Pastushenko, I., Brisebarre, A., Sifrim, A., Fioramonti, M., Revenco, T., Boumahdi, S., Van Keymeulen,
566 A., Brown, D., Moers, V., Lemaire, S., et al. (2018). Identification of the tumour transition states
567 occurring during EMT. Nature *556*, 463–468.

568 Pei, Y.-F., Liu, J., Cheng, J., Wu, W.-D., and Liu, X.-Q. (2019). Silencing of LAMC2 Reverses Epithelial-
569 Mesenchymal Transition and Inhibits Angiogenesis in Cholangiocarcinoma via Inactivation of the
570 Epidermal Growth Factor Receptor Signaling Pathway. Am. J. Pathol. *189*, 1637–1653.

571 Pellinen, T., Blom, S., Sánchez, S., Välimäki, K., Mpindi, J.-P., Azegrouz, H., Strippoli, R., Nieto, R.,
572 Vitón, M., Palacios, I., et al. (2018). ITGB1-dependent upregulation of Caveolin-1 switches TGFβ
573 signalling from tumour-suppressive to oncogenic in prostate cancer. Sci. Rep. *8*, 1–14.

574 Puram, S.V., Parikh, A.S., and Tirosh, I. (2018). Single cell RNA-seq highlights a role for a partial EMT
575 in head and neck cancer. Mol. Cell. Oncol. *5*, e1448244.

576 Ramilowski, J.A., Goldberg, T., Harshbarger, J., Kloppmann, E., Lizio, M., Satagopam, V.P., Itoh, M.,
577 Kawaji, H., Carninci, P., Rost, B., et al. (2015). A draft network of ligand–receptor-mediated
578 multicellular signalling in human. Nat. Commun. *6*, 1–12.

579 Riemondy, K.A., Jansing, N.L., Jiang, P., Redente, E.F., Gillen, A.E., Fu, R., Miller, A.J., Spence, J.R.,
580 Gerber, A.N., Hesselberth, J.R., et al. (2019). Single-cell RNA sequencing identifies TGF-β as a key
581 regenerative cue following LPS-induced lung injury. JCI Insight *4*, e123637.

582 Sadej, R., Romanska, H., Kavanagh, D., Baldwin, G., Takahashi, T., Kalia, N., and Berditchevski, F.
583 (2010). Tetraspanin CD151 Regulates Transforming Growth Factor β Signaling: Implication in
584 Tumor Metastasis. Cancer Res. *70*, 6059–6070.

585 Santibáñez, J.F., Kocić, J., Fabra, A., Cano, A., and Quintanilla, M. (2010). Rac1 modulates TGF-β1-
586 mediated epithelial cell plasticity and MMP9 production in transformed keratinocytes. FEBS Lett.
587 *584*, 2305–2310.

588 Scheel, C., Eaton, E.N., Li, S.H.-J., Chaffer, C.L., Reinhardt, F., Kah, K.-J., Bell, G., Guo, W., Rubin, J.,
589 Richardson, A.L., et al. (2011). Paracrine and Autocrine Signals Induce and Maintain Mesenchymal
590 and Stem Cell States in the Breast. Cell *145*, 926–940.

591 Sha, Y., Haensel, D., Gutierrez, G., Du, H., Dai, X., and Nie, Q. (2019). Intermediate cell states in
592 epithelial-to-mesenchymal transition. Phys. Biol. *16*, 021001.

593 Shirakihara, T., Kawasaki, T., Fukagawa, A., Semba, K., Sakai, R., Miyazono, K., Miyazawa, K., and
594 Saitoh, M. (2013). Identification of integrin α3 as a molecular marker of cells undergoing epithelial-
595 mesenchymal transition and of cancer cells with aggressive phenotypes. Cancer Sci. *104*, 1189–
596 1197.

597 Sigston, E.A.W., and Williams, B.R.G. (2017). An Emergence Framework of Carcinogenesis. Front.
598 Oncol. *7*.

599 Song, J., Wang, W., Wang, Y., Qin, Y., Wang, Y., Zhou, J., Wang, X., Zhang, Y., and Wang, Q. (2019).
600 Epithelial-mesenchymal transition markers screened in a cell-based model and validated in lung
601 adenocarcinoma. BMC Cancer *19*, 680.

602 Tabassum, D.P., and Polyak, K. (2015). Tumorigenesis: it takes a village. Nat. Rev. Cancer *15*, 473–
603 483.

604 Tallima, H., and El Ridi, R. (2018). Arachidonic acid: Physiological roles and potential health benefits
605 – A review. J. Adv. Res. *11*, 33–41.

606 Tam, W.L., Lu, H., Buikhuisen, J., Soh, B.S., Lim, E., Reinhardt, F., Wu, Z.J., Krall, J.A., Bierie, B., Guo, W.,
607 et al. (2013). Protein Kinase C α Is a Central Signaling Node and Therapeutic Target for Breast
608 Cancer Stem Cells. Cancer Cell *24*, 347–364.

609 Tamayo, P., Slonim, D., Mesirov, J., Zhu, Q., Kitareewan, S., Dmitrovsky, E., Lander, E.S., and Golub,
610 T.R. (1999). Interpreting patterns of gene expression with self-organizing maps: Methods and
611 application to hematopoietic differentiation. Proc. Natl. Acad. Sci. *96*, 2907–2912.

612 Thomson, T.M., Balcells, C., and Cascante, M. (2019). Metabolic Plasticity and Epithelial-
613 Mesenchymal Transition. J. Clin. Med. *8*, 967.

614 Tominaga, K., Minato, H., Murayama, T., Sasahara, A., Nishimura, T., Kiyokawa, E., Kanauchi, H.,
615 Shimizu, S., Sato, A., Nishioka, K., et al. (2019). Semaphorin signaling via MICAL3 induces symmetric
616 cell division to expand breast cancer stem-like cells. Proc. Natl. Acad. Sci. *116*, 625–630.

617 Ulgen, E., Ozisik, O., and Sezerman, O.U. (2019). pathfindR: An R Package for Comprehensive
618 Identification of Enriched Pathways in Omics Data Through Active Subnetworks. Front. Genet. *10*.

619 Ungefroren, H., Witte, D., and Lehnert, H. (2018). The role of small GTPases of the Rho/Rac family in
620 TGF-β-induced EMT and cell motility in cancer. Dev. Dyn. *247*, 451–461.

621 Vinayagam, A., Gibson, T.E., Lee, H.-J., Yilmazel, B., Roesel, C., Hu, Y., Kwon, Y., Sharma, A., Liu, Y.-Y.,
622 Perrimon, N., et al. (2016). Controllability analysis of the directed human protein interaction
623 network identifies disease genes and drug targets. Proc. Natl. Acad. Sci. U. S. A. *113*, 4976–4981.

624 Wang, H., Meyer, C.A., Fei, T., Wang, G., Zhang, F., and Liu, X.S. (2013). A systematic approach
625 identifies FOXA1 as a key factor in the loss of epithelial traits during the epithelial-to-mesenchymal
626 transition in lung cancer. BMC Genomics *14*, 680.

627 Wirth, H., von Bergen, M., and Binder, H. (2012). Mining SOM expression portraits: feature selection
628 and integrating concepts of molecular function. BioData Min. *5*, 18.

629 Wu, C.-Y.C., Carpenter, E.S., Takeuchi, K.K., Halbrook, C.J., Peverley, L.V., Bien, H., Hall, J.C., DelGiorno,
630 K.E., Pal, D., Song, Y., et al. (2014). PI3K regulation of RAC1 is required for KRAS-induced pancreatic
631 tumorigenesis in mice. Gastroenterology *147*, 1405-1416.e7.

632 Yang, J., Antin, P., Berx, G., Blanpain, C., Brabletz, T., Bronner, M., Campbell, K., Cano, A., Casanova, J.,
633 Christofori, G., et al. (2020). Guidelines and definitions for research on epithelial–mesenchymal
634 transition. Nat. Rev. Mol. Cell Biol. 1–12.

635 Zhang, J., Tian, X.-J., Zhang, H., Teng, Y., Li, R., Bai, F., Elankumaran, S., and Xing, J. (2014). TGF-β–
636 induced epithelial-to-mesenchymal transition proceeds through stepwise activation of multiple
637 feedback loops. Sci Signal *7*, ra91–ra91.

638 Zhang, J., Lin, X., Wu, L., Huang, J.-J., Jiang, W.-Q., Kipps, T.J., and Zhang, S. (2020). Aurora B induces
639 epithelial–mesenchymal transition by stabilizing Snail1 to promote basal-like breast cancer
640 metastasis. Oncogene *39*, 2550–2567.

641 Zhang, K., Myllymäki, S.-M., Gao, P., Devarajan, R., Kytölä, V., Nykter, M., Wei, G.-H., and Manninen, A.
642 (2017). Oncogenic K-Ras upregulates ITGA6 expression via FOSL1 to induce anoikis resistance and
643 synergizes with αV-Class integrins to promote EMT. Oncogene *36*, 5681–5694.

644

645

646 ## Author contributions

647 **Indranil Paul**: Conceptualization, Methodology, Software, Data curation, Writing – Original draft,
648 Visualization, Investigation, Formal analysis
649 **Dante Bolzan**: Software, Formal analysis
650 **Ahmed Youssef**: Investigation, Software
651 **Keith A Gagnon**: Investigation
652 **Heather Joan Hook**: Investigation
653 **Gopal Karemore**: Software
654 **Michael Uretz John Oliphant**: Investigation
655 **Weiwei Lin**: Investigation
656 **Qian Liu**: Formal analysis
657 **Sadhna Phanse**: Software
658 **Dzmitry Padhorny**: Software
659 **Sergei Kotelnikov**: Software
660 **Carl White**: Software
661 **Guillaume P. Andrieu**: Investigation
662 **Christopher S. Chen**: Investigation
663 **Pingzhao Hu**: Formal analysis
664 **Gerald Denis**: Investigation
665 **Dima Kozakov**: Software
666 **Brian Raught**: Investigation
667 **Trevor Siggers**: Investigation
668 **Stefan Wuchty**: Software, Formal analysis
669 **Senthil Muthuswamy**: Conceptualization, Investigation
670 **Andrew Emili**: Conceptualization, Supervision, Writing – Original draft, Resources, Funding
671 acquisition, Formal analysis

672 ## Acknowledgements

673 We dedicate our sincere gratitude to Stefano Monti, Xarelabos Varelas, Valentina Perissi and Matthew
674 Layne for providing critical feedback on the manuscript. We thank the Microarray and Sequencing
675 Core Facility at Boston University School of Medicine for acquisition of mRNA, miRNA and scRNAseq
676 data.

677 ## Funding

678 S.M., G.D., and A.E. acknowledge joint funding (UO1CA243004) from the NCI program Research
679 Projects in Cancer Systems Biology. The CNSB has generous ongoing support from Boston University.

680 ## Competing interests

681 The authors declare no competing financial interest.

682 # Main figure legends

683 **Figure 1. A multi-dimensional resource on TGFβ-induced EMT**

684 (A) MCF10A cells exposed to TGFβ for indicated time points were used to study the molecular
685 landscapes during EMT.
686 (B) Samples from 3 biological replicates were aliquoted and multiple technologies were
687 employed to quantify various molecular layers.
688 (C) An overview of numbers of molecules quantified in various layers.
689 (D) Expression snapshots of some well-known EMT markers. Heatmaps show log2FC values
690 (relative to Control, adj. *p-value* < 0.05).
691 (E) Variance explained by each layer over 4 principal components.
692 (F) Ridge plot showing differential molecules, as % of total quantified, for each layer.
693 (G) Pie chart showing the overall fraction (in %) of differential molecules (yellow portion)
694 relative to all molecules quantified in each layer.
695 (H) Overlap between established EMT databases (MSigDB, www.gsea-msigdb.org; dbEMT2.0,
696 http://dbemt.bioinfo-minzhao.org) and differential proteins and miRNAs (adj. *p-value* < 0.05;
697 $r^2 \geq 0.6$ & $|\log2FC| \geq 1$) from this study.
698 (I) Differential molecules (proteins, miRNAs, metabolites) were used to assess the number of
699 coherent functional modules, i.e., known interactions between molecules, by employing the
700 Prize-Collecting Steiner Forest algorithm on a network compiled from PathwayCommons,
701 miRTarBase and STITCH.

702 **Figure 2. The topological architecture of EMT**

703 (A) Phylogenetic neighbor-joining tree reveals similarities (=distances) between time points.
704 (B) Combined pseudo-eigenvalues space of all datasets, indicating the contribution of each
705 dataset to the eigenvalue (variance).
706 (C) Matrix correlations between each pair of datasets.
707 (D) Line plots show the distribution of adjusted coefficient of determination (R^2) values between
708 layers as a function of time points.
709 (E) *Left panel.* SOM portraits. Color gradient refers to over- or under-expression of metagenes in
710 each time-point compared to the mean expression level of the metagene in the pool of all time
711 points: red = high, yellow/green = intermediate levels and blue = low (see **STAR Methods** for
712 details). *Middle panel*. Representative examples that appeared among the highest-ranking
713 features (top 1%) in each time-point. *Right panel*. Barplot shows the number of features that
714 were contributed by each layer among the highest-ranking features (top 1%) in time-point.
715 (F) Heatmap depicts sample-wise pathway scores, which were derived from enrichment analysis
716 of active subnetworks using the highest-ranking molecules (top 1%) for each SOM.

717 **Figure 3. Dynamics of TGFβ-induced metabolic adaptations**

718 (A) Barplot showing the 'class' distribution of quantified metabolite features in HMBD. Also
719 shown are the relative proportions of differentially expressed features for each class (*p-value*
720 ≤ 0.01, absolute log2FC ≥ 1).

721 (B) Neighbor-joining tree for the *Metabol* dataset.
722 (C) SOM analysis of the *Metabol* dataset.
723 (D) Top 10% of metabolite features of each SOM were grouped based on clusters in `B` and used
724 for "Network analysis" using MetaboAnalyst (https://www.metaboanalyst.ca).
725 (E) Identified metabolites of AAM pathway in SOM for 4 hours to day 1 were taken and Pearson's
726 correlation computed with known metabolic enzymes (KEGG) quantified in the *Phos* & *WC*
727 datasets.
728 (F) The plot shows enzymes ranked according to their Pearson's correlation with metabolites of
729 AAM pathway, as detected in this study.
730 (G) Schematics of information flow from TGFβ signaling to AAM pathway, mediated by known
731 enzymes. Heatmaps and line plots display 'standardized' expression values.

732 **Figure 4. scRNAseq analysis reveals cellular dynamics and novel TFs for EMT**

733 (A) Violin plots showing expression of well-known EMT hallmarks in each time point.
734 (B) UMAP of scRNAseq by Monocle3. Dots represent single cells and are colored by inferred
735 clusters, while trajectories depict cells during EMT.
736 (C) Heatmap showing the number of cells (in log2 scale) in each cluster of partition P2. Mean
737 expression of some well-known E and M markers in each cluster are also shown.
738 (D) The plot shows all TFs ranked according to their SCENIC score. TF names are shown for the
739 5 TFs with the highest scores and some well-known EMT associated TFs.
740 (E) Tree displays unique TFs identified by SCENIC for each subtype. TFs highlighted in 'bold' are
741 known players in EMT. The genes in the outer circle are representative examples used by
742 SCENIC to infer TF activity.
743 (F) Barplot shows the inferred activities of top 15 TFs based on SCENIC scores in each subtype.
744 (G) Schematics of the human TF-binding array workflow (see **STAR Methods** for details).
745 (H) & (I) Density plots of ∂B-scores of indicated TFs. Two-sided Kolmogorov-Smirnov test was
746 performed to evaluate the significance of distribution differences between Control and TGFβ
747 treated conditions.

748 **Figure 5. Spatial regulation of proteins and intercellular communication**

749 (A) The schematic summarizes Pearson's coefficients between overlapping proteins of the
750 indicated layers. Each pie chart depicts the fraction of differential proteins (orange slice) with
751 respect to all proteins quantified in the layer.
752 (B) The plot displays top 25 Class I proteins. Each pair is represented by a different shape.
753 (C) Expression profiles of top 3 Class I proteins. Each colored line represents a molecular layer.
754 (D) The plot displays top 25 Class II proteins. Each pair is represented by a different shape.
755 (E) Expression profiles of top 3 Class II proteins. Each colored line represents a molecular layer.
756 (F) Expression profiles of BRD2 and BRD4 in various layers. Legend as in E.
757 (G) Density plots of ∂B-scores of indicated co-factors. Two-sided Kolmogorov-Smirnov test was
758 performed to evaluate the significance of difference in distributions.
759 (H) Phase-contrast images after 6 days of TGFβ treatment in presence or absence of active JQ-1
760 (100 nM) or its inactive analogue.
761 (I) Expression profile of SCRIB in various layers. Legend as in E.

762 (J) PPI network of SCRIB interactors identified using BioID.
763 (K) Immunoblots showing interactions of a few SCRIB partners identified using BioID.
764 (L) Schematics of analysis pipeline for discovering active L-R pairs (see **STAR Methods**).
765 (M) Heatmap showing combined log2FCs of L-R pairs in the *Sec* and *Mem/Glyco* datasets.
766 (N) Network plot showing L-R interactions detected between different P2 cell clusters.
767 (O) Scatter plot of correlations between indicated gene-pairs in Breast invasive carcinoma
768 samples. Regression line is shown in red.

769 **Figure 6. Phosphoproteome dynamics during EMT**

770 (A) Fraction of detected p-sites on a protein that are regulated during EMT.
771 (B) Detected p-sites on VIM and their expression during EMT. The gray lines indicate all p-sites
772 that are catalogued in PhosphoSitePlus database.
773 (C) Distribution of Pearson's correlation between expression of proteins and p-sites detected on
774 them.
775 (D) Schematic showing two examples each where expression of proteins and p-sites showed
776 either low (≤–0.1; CDS2, CBX1) or high (≥0.4; MISP, MICAL3) correlation.
777 (E) Gene ontology enrichment of genes with at least a single regulated p-site at any time point.
778 (F) Distribution of Pearson's correlation between expression of proteins detected in *Nuc* layer
779 and the p-sites detected on them in the *Phos* layer. A few EMT hallmarks are highlighted.
780 (G) Heatmaps of expression profiles of indicated molecules in *Nuc* and *Phos* layers.
781 (H) Structural model of MICAL3 p-sites, NLS and Importin-α.
782 (I) Ternary plot of kinase activity scores binned into 3 broad stages of EMT, i.e., E, ICS, and M.
783 (J) and (K) *Top*. Expression of PRKCA or AURKB as detected in various layers. *Bottom*. Pathway
784 enrichment of all differential substrates of PRKCA or AURKB detected in our dataset.

785 **Figure 7. Integrative systems causal model of EMT**

786 (A) Schematics of causal modeling workflow. Non-redundant genes with most significant
787 expression profiles (Hotelling's T^2 statistic) were used. CausalPath-estimated logical
788 networks were used to augment a custom-built confidence-weighted scaffold interactome
789 which was then used to solve the Steiner Forest problem using the OmicsIntegrator software.
790 Only differential molecules (relative to Control, FDR adj.*p-value* ≤ 0.05, |log2FC| ≥ 1) were
791 considered as 'prizes'.
792 (B) Overlap between EMT databases and 'controllers' identified in this study.
793 (C) Overlap between EMT databases and 'non-controllers' identified in this study.
794 (D) Kaplan-Meier plots comparing prognostic performance of MSigDB hallmarks and
795 'controllers' identified in this study.
796 (E) A simplified schematic showing the hierarchical relationships between several bottleneck
797 genes at different stages of EMT, as indicated.
798 (F) Workflow for morphometric screening of drug combinations.
799 (G) Barplot of results of above experiment indicates varying degrees of synergy or antagonism
800 between inhibitors, in influencing EMT-associated changes in cell shape (eccentricity). Error
801 bars indicate spread of datapoints across all quantified cells in each condition.

802 (H) 3D ducts were seeded with stable MCF10A$^{PIK3CA\text{-}H1047R}$ cells and treated with Sonidegib and
803 Autocamtide for 3 days. Area of invading cells and average distance traveled away from the
804 ducts as compared to DMSO treated controls were quantified using ImageJ (n=6 devices).

805 Supplementary figure legends

806 **Figure S1. Related to Figure 1. A multi-dimensional resource on TGFβ-induced EMT**

807 (A) TGFβ treatments were staggered, at defined time periods, such that all plates were harvested
808 at the same time. Cells were serum starved for 16 hours before harvesting.
809 (B) Phase-contrast images of MCF10A cells at different time points. Scale bar = 100 μm.
810 (C) For maximizing efficiency while maintaining compatibility with technology-specific
811 protocols, after harvesting cells were collected in 4 aliquots per replicate, as shown.
812 Conditioned media were also collected.
813 (D) Upper panel – barplot showing percentage of quantified proteins with annotation in the
814 'Cellular Component' category. Lower panel – boxplot showing intensity values (log2) of
815 proteins (=markers) commonly used to assess sub-cellular fractionation purity. Box edges
816 correspond to 25th and 75th percentiles, whiskers include extreme data points.
817 (E) Cumulative distribution (%) of Pearson's coefficients across the samples (= time points).
818 Significant overlap between the 3 biological replicates, shown as 3 colors, indicates high
819 reproducibility.
820 (F) Heatmaps of molecular expression profiles of indicated layers. The mean of all quantified
821 molecules across the 3 replicates was used.
822 (G) Violin plots showing the spread of log2FCs of molecules at each time point (relative to
823 Control) for each layer.

824 **Figure S2. Related to Figure 2. The topological architecture of EMT**

825 (A) PCA of the various molecular layers. Time points are shown with different shapes and
826 colors. Points with similar shape/color indicate biological replicates.
827 (B) The population map presents the number of genes mapped to each individual metagene.
828 (C) The plot summarizes co-variance structure of datasets at the metagene level.
829 (D) The plot shows correlation of expression patterns of individual genes and the metagenes in
830 which they are contained.
831 (E) Temporal expression profiles of a few example genes identified in SOM analysis. Each colored
832 line represents a molecular layer, as shown.
833 (F) Temporal expression profiles of a few example genes enlisted as 'EMT hallmarks' in MSigDB
834 database. Each colored line represents a molecular layer, as shown.

835 **Figure S3. Related to Figure 3. Dynamics of TGFβ-induced metabolic adaptations**

836 (A) The heatmap displays the results of active subnetwork analysis using differential molecules
837 in *WC* and *Phos* datasets.
838 (B) – (D) Metabolite-metabolite interaction networks, using MetaboAnalyst, for indicated
839 clusters. High connectivity indicates co-regulation of functionally related metabolites.

840 **Figure S4. Related to Figure 4. scRNAseq analysis reveals cellular dynamics and novel TFs for**
841 **EMT**

842 (A) An outline of the QC pipeline employed for scRNAseq data analysis.
843 (B) The plot shows top 25 most expressed genes. Each row corresponds to a gene and each bar
844 corresponds to the expression of the gene in single cells.
845 (C) Expression of indicated genes in *mRNA* layer.
846 (D) Developmental trajectories of MCF10A cells in response to TGFβ, inferred by Monocle3.
847 Clusters are indicated by colors.
848 (E) Heatmap showing aggregate expression of groups of genes (=Modules) with similar
849 expression pattern across the *partitions*, by Monocle3. Modules 9/12 were highly expressed
850 in P1/P3 and were enriched for 'Cell cycle' related GO annotations.

851 **Figure S5. Related to Figure 5. Spatial regulation of proteins and intercellular communication**

852 (A) The plot shows number of common genes (intersection size, *y* axis) between layers as
853 indicated. Only differential genes in each layer ('Set size', FDR ≤ 0.05; adj. *p-value* ≤ 0.05; r^2 ≥
854 0.6 & |log2FC|, relative to Control, of ≥ 1) were considered for the analysis.
855 (B) Schematics of the BioID experiment performed to discover novel SCRIB partners induced by
856 TGFβ signaling.
857 (C) Circos plot showing L-R interactions between the P2 clusters.
858 (D) UMAP plots of scRNAseq data highlighting the co-expression patterns of MMP7 and CD44.

859 **Figure S6. Related to Figure 6. Phosphoproteome dynamics during EMT**

860 (A) An outline of QC pipeline for *Phos* data analysis.
861 (B) Enrichment efficiency for TiO_2 workflow employed for the study.
862 (C) About 74% of all detected p-sites were reliably localized (=Class I) by MaxQuant.
863 (D) Quantifications of p-sites were achieved with a dynamic range of 10^6 orders of magnitude.
864 (E) Proportions of number of phosphate moieties in each detected p-site.
865 (F) Number of phosphoproteins regulated over the time course.
866 (G) Magnitudes of log2FC values for p-sites over the time course.
867 (H) The plot shows all kinases ranked according to their KSEA enrichment. Mean of |z-score|
868 values over all time points were taken.

869 **Figure S7. Related to Figure 7. Integrative systems causal model of EMT**

870 (A) A subgraph showing the signaling context of well-known EMT players 'queried' on the EMT
871 network.
872 (B) A snapshot of the companion website which can be interactively and freely accessed at
873 https://www.bu.edu/dbin/cnsb/emtapp/.

Figure 1

A Experimental design and premise

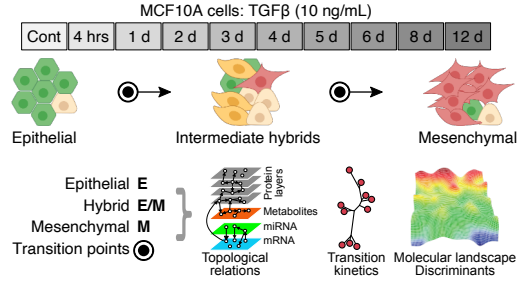

B Data acquisition, technologies and platforms

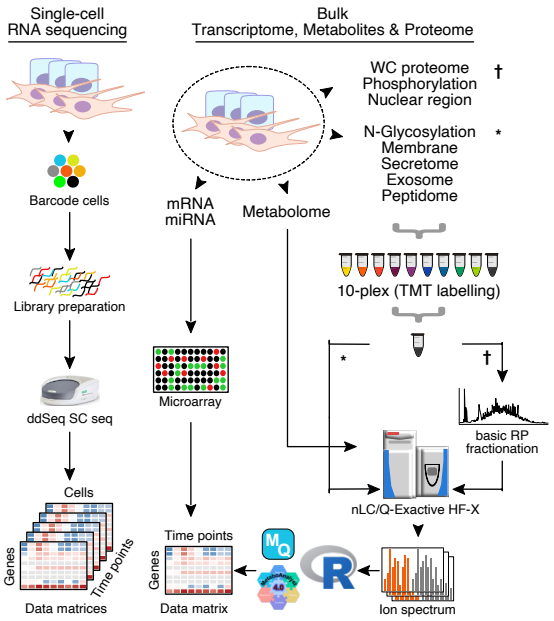

C Datasets (this study, 10 time points)

Proteomics Component	Peptides	Genes (signif. up/dn) **	PTM sites * (signif. up/dn) **
Whole cell proteome (WC)	552,716	6,540 (403/470)	--
Nuclear region (Nuc)	286,162	4,198 (298/259)	--
Membrane (Mem)	35,870	2,223 (149/131)	--
Peptidome (Pep)	735	202 (31/31)	--
Secretome (Sec)	27,136	1,133 (247/200)	--
Extracellular vesicles (EV)	20,438	1,209 (149/123)	--
Glycosylated proteins (Glyco)	6696	590 (17/26)	--
Phosphorylation (Phos)	149,469	2,254	8,741 (1,536/1,602)
Total unique proteins	--	7,632	--

Transcriptomics Single cell	Matrix	Total RNA	Genes (signif. up/dn)
Number of cells ***	1,913	mRNA	23,787 (2,441/1,993)
mRNA	9,785	mi-RNA	2,574 (178/118)

Metabolomics	Features (MS1 peaks)	HMDB indexed	KEGG indexed
Features (Level 2) ****	27,759	4,259 (610/468)	545 (65/59)

* Unique PTM sites remaining after QC steps; ** relative to `Control`; absolute log2FC ≥ 1, FDR ≤ 0.05, r^2 ≥ 0.6;
*** Number of cells & genes remaining after QC steps **** Level 2 identifications (Salek et al., 2013)

D MultiOmic profiles of EMT markers

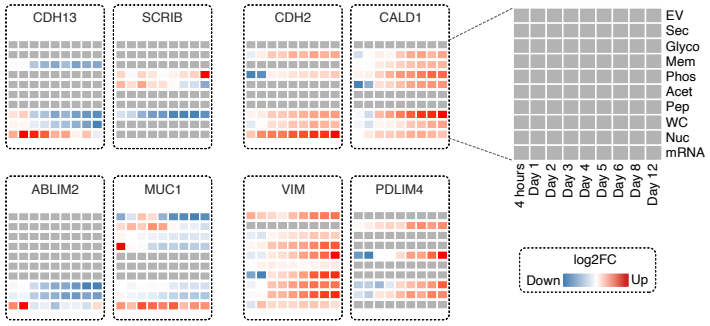

E Variance contribution

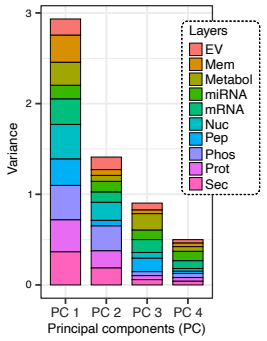

F Differentially expressed features

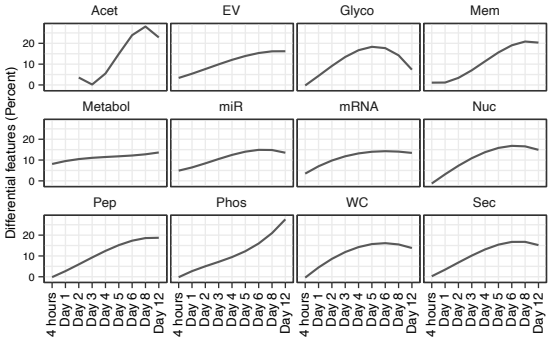

G Differential molecules as % of total detected

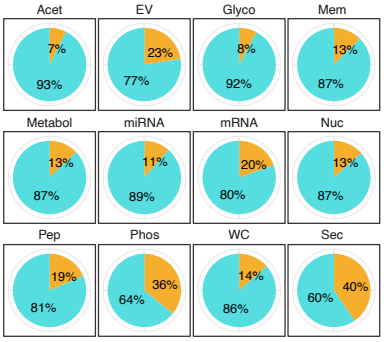

H Comparison to current knowledge

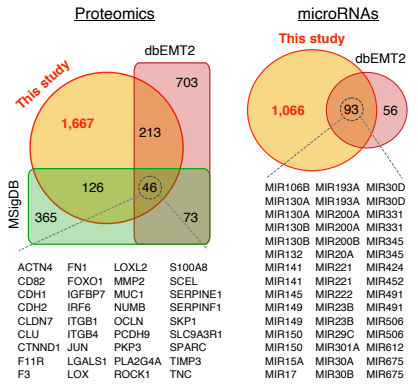

I Enhanced discovery of coherent functional modules

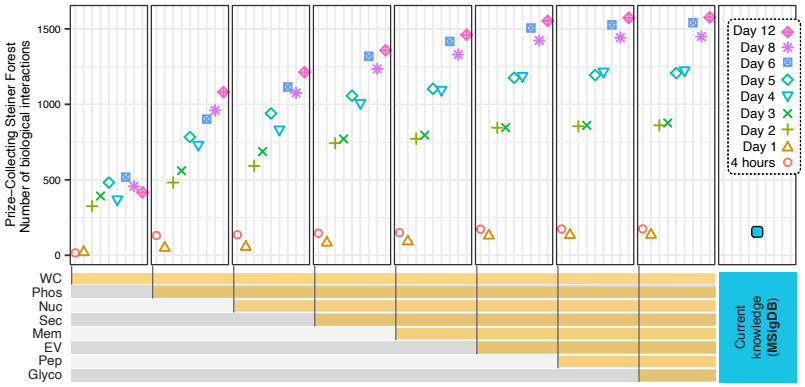

Figure 2

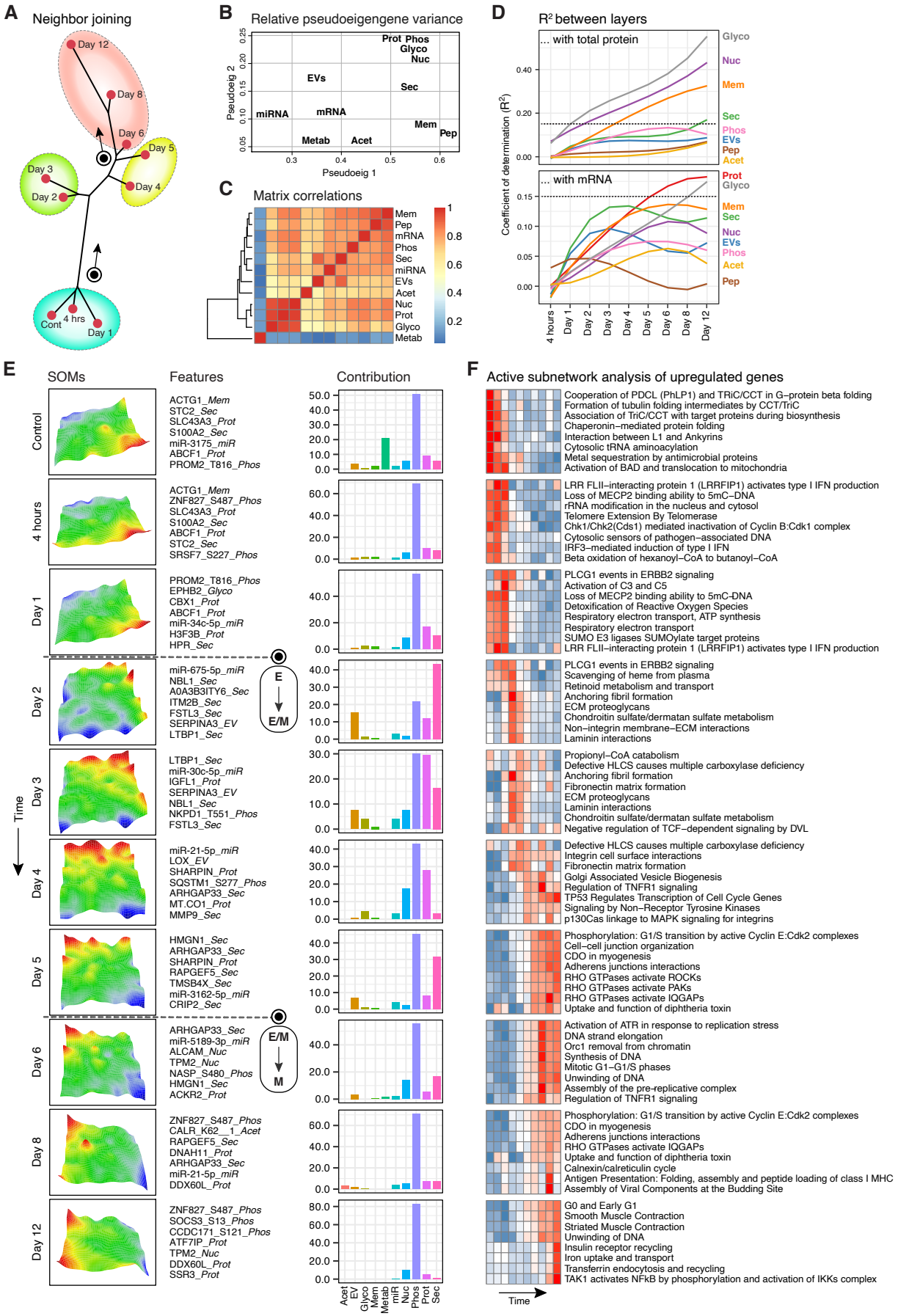
A
Neighbor joining
Day 12
Day 8
Day 6
Day 5
Day 3
Day 2
Day 4
Cont
4 hrs
Day 1
B
Relative pseudoeigengene variance
Pseudoeig 2
Pseudoeig 1
Prot Phos
Glyco
Nuc
EVs
Sec
miRNA
mRNA
Mem
Pep
Metab
Acet
C
Matrix correlations
Mem
Pep
mRNA
Phos
Sec
miRNA
EVs
Acet
Nuc
Prot
Glyco
Metab
D
R² between layers
... with total protein
... with mRNA
Coefficient of determination (R²)
Glyco
Nuc
Mem
Sec
Phos
EVs
Pep
Acet
Prot
4 hours
Day 1
Day 2
Day 3
Day 4
Day 5
Day 6
Day 8
Day 12
E
SOMs
Features
Contribution
Control
4 hours
Day 1
Day 2
Day 3
Day 4
Day 5
Day 6
Day 8
Day 12
Time
ACTG1_Mem
STC2_Sec
SLC43A3_Prot
S100A2_Sec
miR-3175_miR
ABCF1_Prot
PROM2_T816_Phos
ACTG1_Mem
ZNF827_S487_Phos
SLC43A3_Prot
S100A2_Sec
ABCF1_Prot
STC2_Sec
SRSF7_S227_Phos
PROM2_T816_Phos
EPHB2_Glyco
CBX1_Prot
ABCF1_Prot
miR-34c-5p_miR
H3F3B_Prot
HPR_Sec
miR-675-5p_miR
NBL1_Sec
A0A3B3ITY6_Sec
ITM2B_Sec
FSTL3_Sec
SERPINA3_EV
LTBP1_Sec
E
E/M
LTBP1_Sec
miR-30c-5p_miR
IGFL1_Prot
SERPINA3_EV
NBL1_Sec
NKPD1_T551_Phos
FSTL3_Sec
miR-21-5p_miR
LOX_EV
SHARPIN_Prot
SQSTM1_S277_Phos
ARHGAP33_Sec
MT.CO1_Prot
MMP9_Sec
HMGN1_Sec
ARHGAP33_Sec
SHARPIN_Prot
RAPGEF5_Sec
TMSB4X_Sec
miR-3162-5p_miR
CRIP2_Sec
ARHGAP33_Sec
miR-5189-3p_miR
ALCAM_Nuc
TPM2_Nuc
NASP_S480_Phos
HMGN1_Sec
ACKR2_Prot
E/M
M
ZNF827_S487_Phos
CALR_K62__1_Acet
RAPGEF5_Sec
DNAH11_Prot
ARHGAP33_Sec
miR-21-5p_miR
DDX60L_Prot
ZNF827_S487_Phos
SOCS3_S13_Phos
CCDC171_S121_Phos
ATF7IP_Prot
TPM2_Nuc
DDX60L_Prot
SSR3_Prot
Acet
EV
Glyco
Mem
Metab
miR
Nuc
Phos
Prot
Sec
F
Active subnetwork analysis of upregulated genes
Cooperation of PDCL (PhLP1) and TRiC/CCT in G−protein beta folding
Formation of tubulin folding intermediates by CCT/TriC
Association of TriC/CCT with target proteins during biosynthesis
Chaperonin−mediated protein folding
Interaction between L1 and Ankyrins
Cytosolic tRNA aminoacylation
Metal sequestration by antimicrobial proteins
Activation of BAD and translocation to mitochondria
LRR FLII−interacting protein 1 (LRRFIP1) activates type I IFN production
Loss of MECP2 binding ability to 5mC−DNA
rRNA modification in the nucleus and cytosol
Telomere Extension By Telomerase
Chk1/Chk2(Cds1) mediated inactivation of Cyclin B:Cdk1 complex
Cytosolic sensors of pathogen−associated DNA
IRF3−mediated induction of type I IFN
Beta oxidation of hexanoyl−CoA to butanoyl−CoA
PLCG1 events in ERBB2 signaling
Activation of C3 and C5
Loss of MECP2 binding ability to 5mC-DNA
Detoxification of Reactive Oxygen Species
Respiratory electron transport, ATP synthesis
Respiratory electron transport
SUMO E3 ligases SUMOylate target proteins
LRR FLII−interacting protein 1 (LRRFIP1) activates type I IFN production
PLCG1 events in ERBB2 signaling
Scavenging of heme from plasma
Retinoid metabolism and transport
Anchoring fibril formation
ECM proteoglycans
Chondroitin sulfate/dermatan sulfate metabolism
Non−integrin membrane−ECM interactions
Laminin interactions
Propionyl−CoA catabolism
Defective HLCS causes multiple carboxylase deficiency
Anchoring fibril formation
Fibronectin matrix formation
ECM proteoglycans
Laminin interactions
Chondroitin sulfate/dermatan sulfate metabolism
Negative regulation of TCF−dependent signaling by DVL
Defective HLCS causes multiple carboxylase deficiency
Integrin cell surface interactions
Fibronectin matrix formation
Golgi Associated Vesicle Biogenesis
Regulation of TNFR1 signaling
TP53 Regulates Transcription of Cell Cycle Genes
Signaling by Non−Receptor Tyrosine Kinases
p130Cas linkage to MAPK signaling for integrins
Phosphorylation: G1/S transition by active Cyclin E:Cdk2 complexes
Cell−cell junction organization
CDO in myogenesis
Adherens junctions interactions
RHO GTPases activate ROCKs
RHO GTPases activate PAKs
RHO GTPases activate IQGAPs
Uptake and function of diphtheria toxin
Activation of ATR in response to replication stress
DNA strand elongation
Orc1 removal from chromatin
Synthesis of DNA
Mitotic G1−G1/S phases
Unwinding of DNA
Assembly of the pre-replicative complex
Regulation of TNFR1 signaling
Phosphorylation: G1/S transition by active Cyclin E:Cdk2 complexes
CDO in myogenesis
Adherens junctions interactions
RHO GTPases activate IQGAPs
Uptake and function of diphtheria toxin
Calnexin/calreticulin cycle
Antigen Presentation: Folding, assembly and peptide loading of class I MHC
Assembly of Viral Components at the Budding Site
G0 and Early G1
Smooth Muscle Contraction
Striated Muscle Contraction
Unwinding of DNA
Insulin receptor recycling
Iron uptake and transport
Transferrin endocytosis and recycling
TAK1 activates NFkB by phosphorylation and activation of IKKs complex
Time

Figure 3

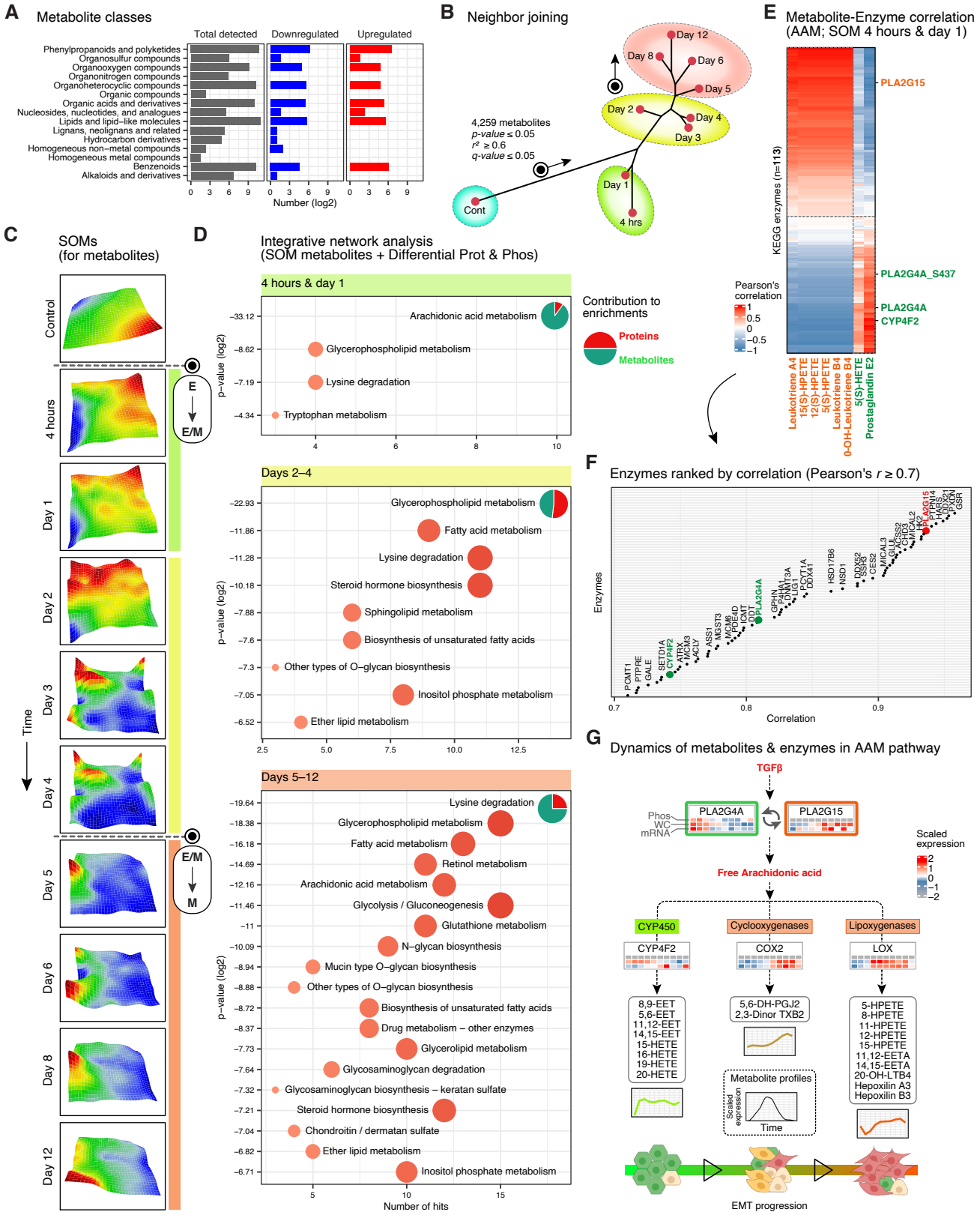
A
Metabolite classes
Total detected
Downregulated
Upregulated
Phenylpropanoids and polyketides
Organosulfur compounds
Organooxygen compounds
Organonitrogen compounds
Organoheterocyclic compounds
Organic compounds
Organic acids and derivatives
Nucleosides, nucleotides, and analogues
Lipids and lipid–like molecules
Lignans, neolignans and related
Hydrocarbon derivatives
Homogeneous non–metal compounds
Homogeneous metal compounds
Benzenoids
Alkaloids and derivatives
Number (log2)
B
Neighbor joining
4,259 metabolites
p-value ≤ 0.05
r² ≥ 0.6
q-value ≤ 0.05
Cont
Day 1
4 hrs
Day 2
Day 3
Day 4
Day 5
Day 6
Day 8
Day 12
E
Metabolite-Enzyme correlation
(AAM; SOM 4 hours & day 1)
KEGG enzymes (n=113)
PLA2G15
PLA2G4A_S437
PLA2G4A
CYP4F2
Pearson's correlation
Leukotriene A4
15(S)-HPETE
12(S)-HPETE
5(S)-HPETE
Leukotriene B4
0-OH-Leukotriene B4
5(S)-HETE
Prostaglandin E2
C
SOMs
(for metabolites)
Control
4 hours
Day 1
Day 2
Day 3
Day 4
Day 5
Day 6
Day 8
Day 12
Time
E
E/M
M
D
Integrative network analysis
(SOM metabolites + Differential Prot & Phos)
4 hours & day 1
Arachidonic acid metabolism
Glycerophospholipid metabolism
Lysine degradation
Tryptophan metabolism
p–value (log2)
Contribution to enrichments
Proteins
Metabolites
Days 2–4
Glycerophospholipid metabolism
Fatty acid metabolism
Lysine degradation
Steroid hormone biosynthesis
Sphingolipid metabolism
Biosynthesis of unsaturated fatty acids
Other types of O–glycan biosynthesis
Inositol phosphate metabolism
Ether lipid metabolism
Days 5–12
Lysine degradation
Glycerophospholipid metabolism
Fatty acid metabolism
Retinol metabolism
Arachidonic acid metabolism
Glycolysis / Gluconeogenesis
Glutathione metabolism
N–glycan biosynthesis
Mucin type O–glycan biosynthesis
Other types of O–glycan biosynthesis
Biosynthesis of unsaturated fatty acids
Drug metabolism – other enzymes
Glycerolipid metabolism
Glycosaminoglycan degradation
Glycosaminoglycan biosynthesis – keratan sulfate
Steroid hormone biosynthesis
Chondroitin / dermatan sulfate
Ether lipid metabolism
Inositol phosphate metabolism
Number of hits
F
Enzymes ranked by correlation (Pearson's r ≥ 0.7)
Enzymes
Correlation
G
Dynamics of metabolites & enzymes in AAM pathway
TGFβ
Phos
WC
mRNA
PLA2G4A
PLA2G15
Scaled expression
Free Arachidonic acid
CYP450
Cyclooxygenases
Lipoxygenases
CYP4F2
COX2
LOX
8,9-EET
5,6-EET
11,12-EET
14,15-EET
15-HETE
16-HETE
19-HETE
20-HETE
5,6-DH-PGJ2
2,3-Dinor TXB2
5-HPETE
8-HPETE
11-HPETE
12-HPETE
15-HPETE
11,12-EETA
14,15-EETA
20-OH-LTB4
Hepoxilin A3
Hepoxilin B3
Metabolite profiles
Time
EMT progression

Figure 4

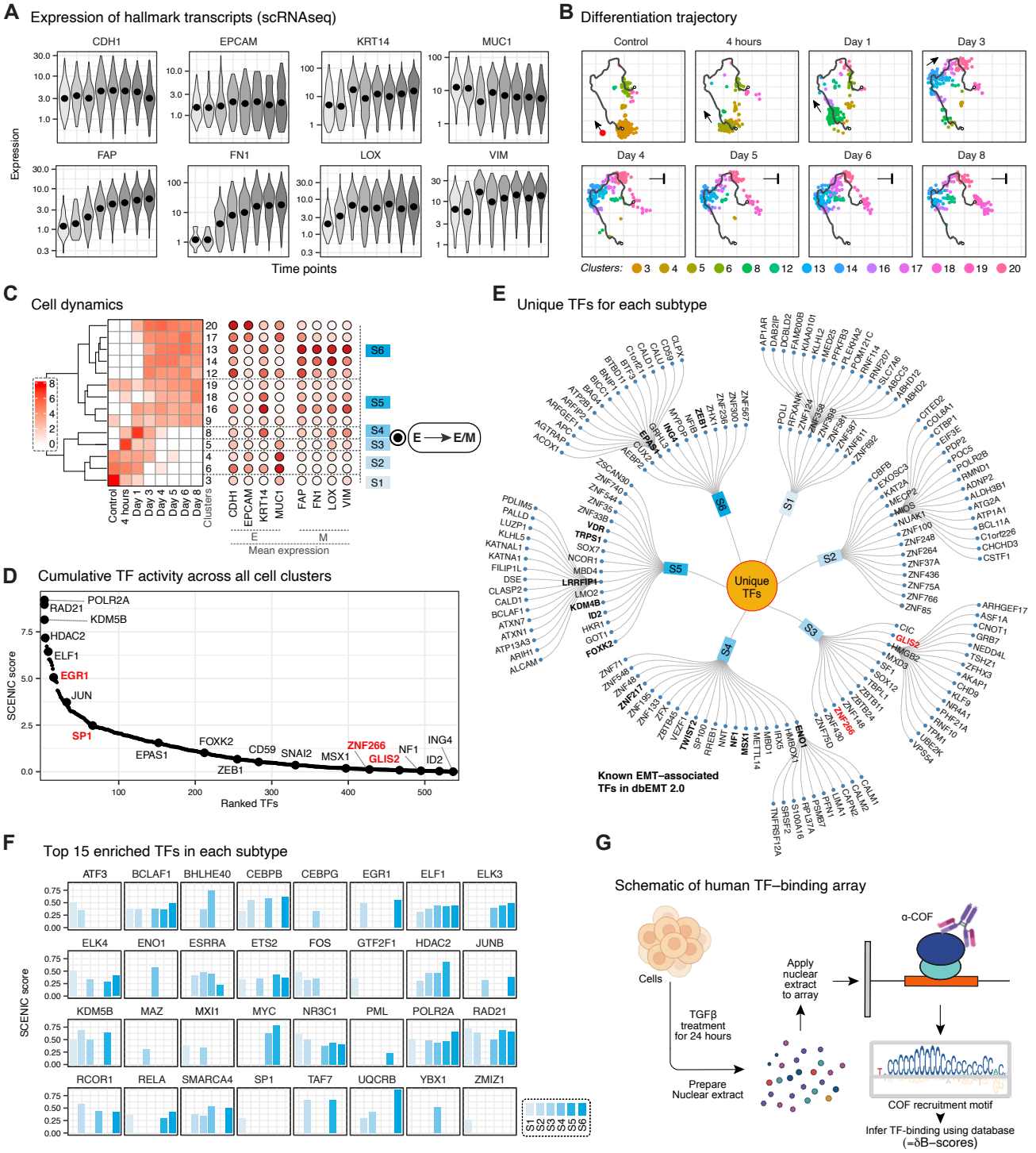
A
Expression of hallmark transcripts (scRNAseq)
CDH1
EPCAM
KRT14
MUC1
FAP
FN1
LOX
VIM
Expression
Time points
B
Differentiation trajectory
Control
4 hours
Day 1
Day 3
Day 4
Day 5
Day 6
Day 8
Clusters: 3 4 5 6 8 12 13 14 16 17 18 19 20
C
Cell dynamics
S6
S5
S4
S3
S2
S1
E → E/M
Control
4 hours
Day 1
Day 3
Day 4
Day 5
Day 6
Day 8
Clusters
CDH1
EPCAM
KRT14
MUC1
FAP
FN1
LOX
VIM
E
M
Mean expression
D
Cumulative TF activity across all cell clusters
SCENIC score
Ranked TFs
POLR2A
RAD21
KDM5B
HDAC2
ELF1
EGR1
JUN
SP1
EPAS1
FOXK2
ZEB1
CD59
SNAI2
MSX1
ZNF266
GLIS2
NF1
ID2
ING4
E
Unique TFs for each subtype
Unique TFs
S1
S2
S3
S4
S5
S6
Known EMT–associated TFs in dbEMT 2.0
F
Top 15 enriched TFs in each subtype
SCENIC score
ATF3
BCLAF1
BHLHE40
CEBPB
CEBPG
EGR1
ELF1
ELK3
ELK4
ENO1
ESRRA
ETS2
FOS
GTF2F1
HDAC2
JUNB
KDM5B
MAZ
MXI1
MYC
NR3C1
PML
POLR2A
RAD21
RCOR1
RELA
SMARCA4
SP1
TAF7
UQCRB
YBX1
ZMIZ1
S1 S2 S3 S4 S5 S6
G
Schematic of human TF–binding array
Cells
TGFβ treatment for 24 hours
Prepare Nuclear extract
Apply nuclear extract to array
α-COF
COF recruitment motif
Infer TF-binding using database (=δB–scores)
H
δB–score distributions
Transcription factors
ZNF263
SP1
GLIS2
p-val ≤ 0.006
D ≥ 0.27
p-val ≤ 0.007
D ≥ 0.34
p-val ≤ 0.000
D ≥ 0.45
δB–scores
Recovered
Consensus
I
δB–score distributions
Transcription factors
PAX1
GCM2
EGR1
p-val ≤ 0.001
D ≥ 0.32
p-val ≤ 0.120
D ≥ 0.25
p-val ≤ 0.092
D ≥ 0.23
δB–scores
Recovered
Consensus

Figure 5

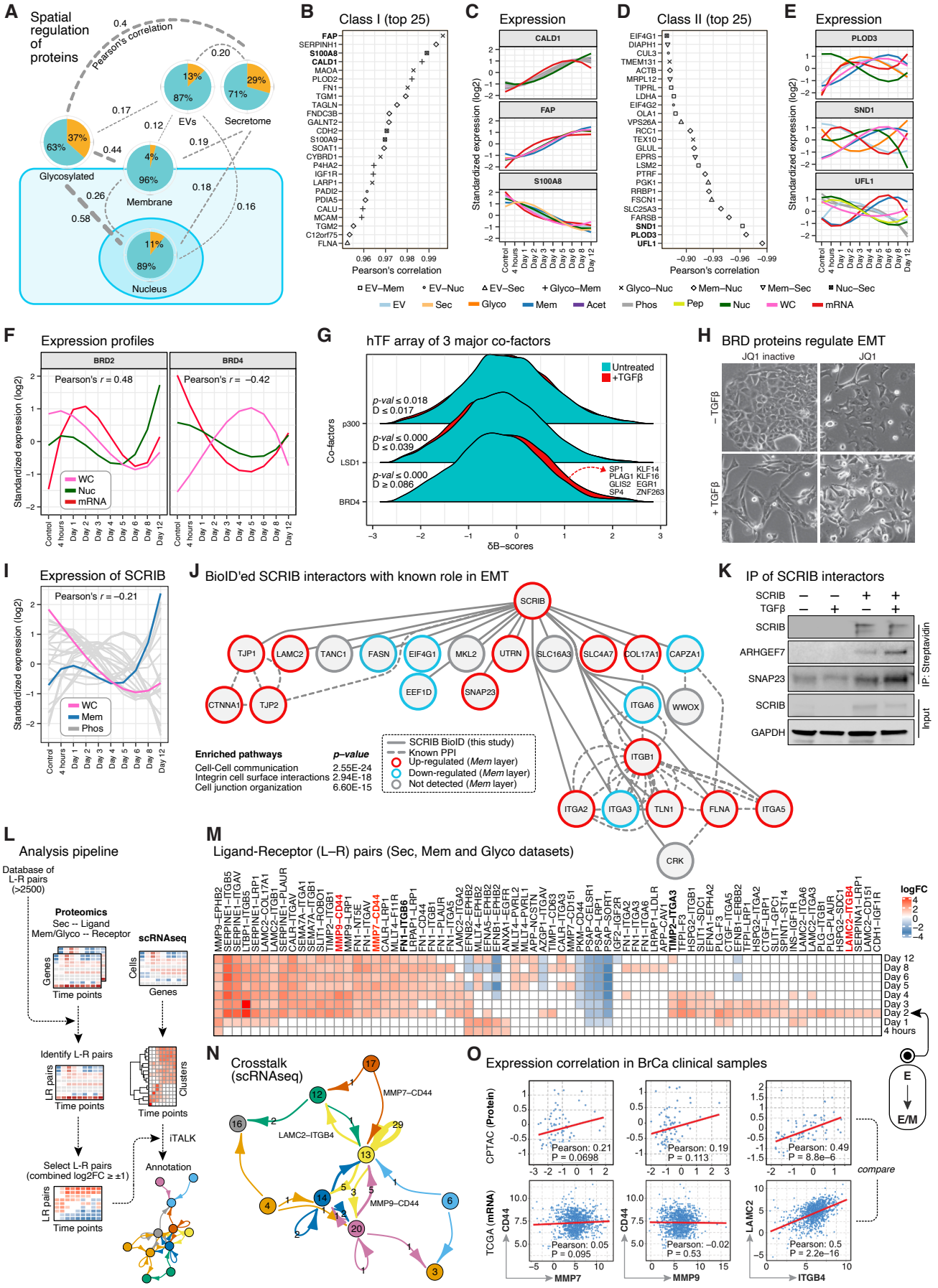
A
Spatial regulation of proteins
Pearson's correlation
EVs
Secretome
Glycosylated
Membrane
Nucleus
B
Class I (top 25)
Pearson's correlation
C
Expression
CALD1
FAP
S100A8
Standardized expression (log2)
D
Class II (top 25)
Pearson's correlation
E
Expression
PLOD3
SND1
UFL1
EV–Mem
EV–Nuc
EV–Sec
Glyco–Mem
Glyco–Nuc
Mem–Nuc
Mem–Sec
Nuc–Sec
EV
Sec
Glyco
Mem
Acet
Phos
Pep
Nuc
WC
mRNA
F
Expression profiles
BRD2
BRD4
Pearson's r = 0.48
Pearson's r = −0.42
WC
Nuc
mRNA
G
hTF array of 3 major co-factors
Untreated
+TGFβ
Co-factors
p300
LSD1
BRD4
δB−scores
H
BRD proteins regulate EMT
JQ1 inactive
JQ1
− TGFβ
+ TGFβ
I
Expression of SCRIB
Pearson's r = −0.21
WC
Mem
Phos
J
BioID'ed SCRIB interactors with known role in EMT
SCRIB
Enriched pathways
p−value
Cell-Cell communication 2.55E-24
Integrin cell surface interactions 2.94E-18
Cell junction organization 6.60E-15
SCRIB BioID (this study)
Known PPI
Up-regulated (Mem layer)
Down-regulated (Mem layer)
Not detected (Mem layer)
K
IP of SCRIB interactors
SCRIB
TGFβ
ARHGEF7
SNAP23
GAPDH
IP: Streptavidin
Input
L
Analysis pipeline
Database of L-R pairs (>2500)
Proteomics
Sec -- Ligand
Mem/Glyco -- Receptor
scRNAseq
Genes
Time points
Cells
Identify L-R pairs
LR pairs
Clusters
iTALK
Annotation
Select L-R pairs (combined log2FC ≥ ±1)
M
Ligand-Receptor (L–R) pairs (Sec, Mem and Glyco datasets)
logFC
Day 12
Day 8
Day 6
Day 5
Day 4
Day 3
Day 2
Day 1
4 hours
N
Crosstalk (scRNAseq)
MMP7–CD44
LAMC2–ITGB4
MMP9–CD44
O
Expression correlation in BrCa clinical samples
CPTAC (Protein)
TCGA (mRNA)
Pearson: 0.21
P = 0.0698
Pearson: 0.19
P = 0.113
Pearson: 0.49
P = 8.8e−6
Pearson: 0.05
P = 0.095
Pearson: −0.02
P = 0.53
Pearson: 0.5
P = 2.2e−16
CD44
LAMC2
MMP7
MMP9
ITGB4
compare
E
E/M

Figure 6

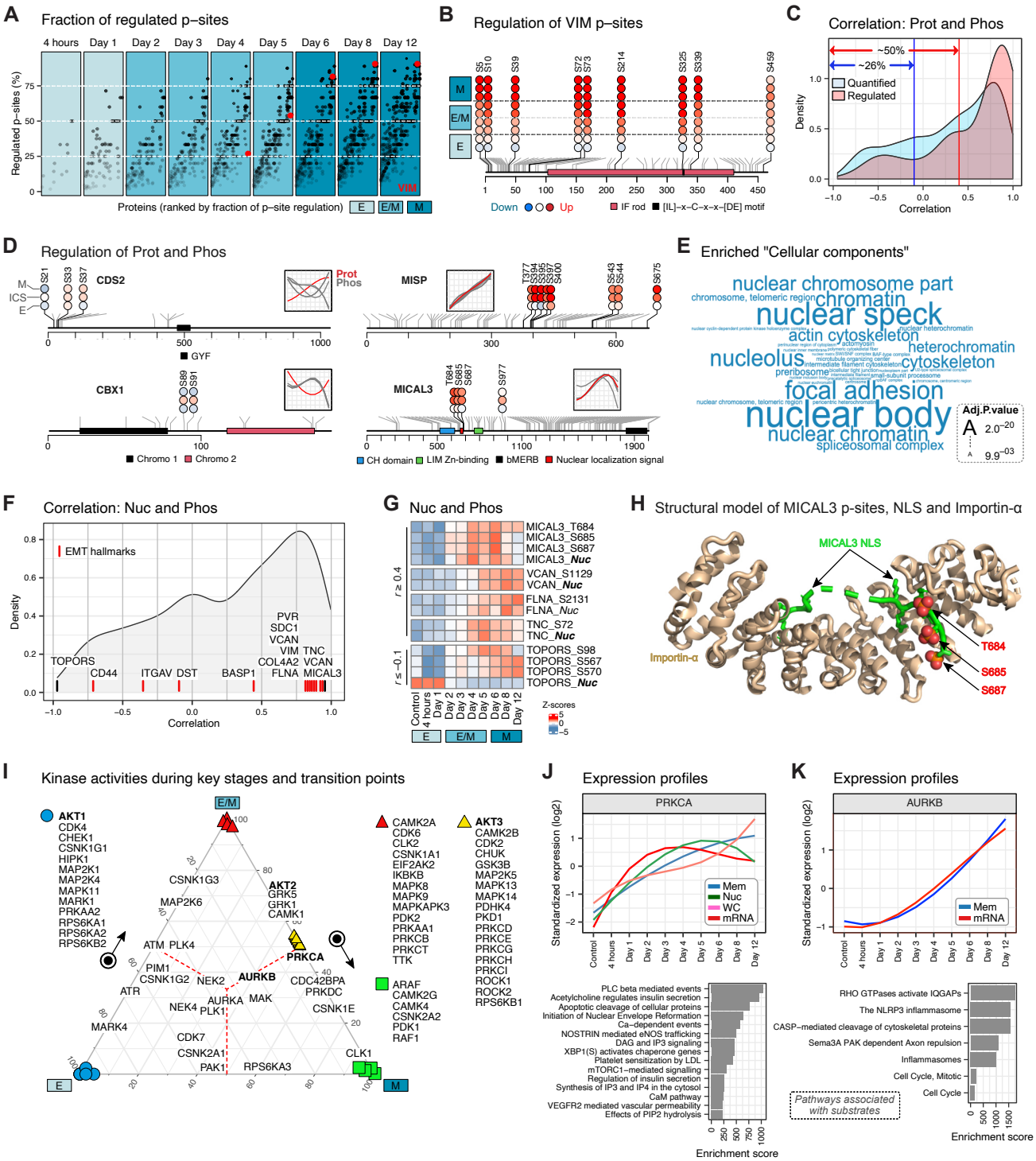
A
Fraction of regulated p–sites
4 hours
Day 1
Day 2
Day 3
Day 4
Day 5
Day 6
Day 8
Day 12
Regulated p–sites (%)
VIM
Proteins (ranked by fraction of p–site regulation)
E
E/M
M
B
Regulation of VIM p–sites
S5
S10
S39
S72
S73
S214
S325
S339
S459
M
E/M
E
Down
Up
IF rod
[IL]–x–C–x–x–[DE] motif
C
Correlation: Prot and Phos
~50%
~26%
Quantified
Regulated
Density
Correlation
D
Regulation of Prot and Phos
CDS2
S21
S33
S37
M
ICS
E
Prot
Phos
GYF
MISP
T377
S394
S396
S397
S400
S543
S544
S675
CBX1
S89
S91
Chromo 1
Chromo 2
MICAL3
T684
S685
S687
S977
CH domain
LIM Zn-binding
bMERB
Nuclear localization signal
E
Enriched "Cellular components"
nuclear chromosome part
chromosome, telomeric region
chromatin
nuclear speck
actin cytoskeleton
heterochromatin
nucleolus
cytoskeleton
preribosome
focal adhesion
nuclear body
nuclear chromatin
spliceosomal complex
Adj.P.value
F
Correlation: Nuc and Phos
EMT hallmarks
Density
Correlation
TOPORS
CD44
ITGAV
DST
BASP1
PVR
SDC1
VCAN
VIM
TNC
COL4A2
VCAN
FLNA
MICAL3
G
Nuc and Phos
MICAL3_T684
MICAL3_S685
MICAL3_S687
MICAL3_Nuc
VCAN_S1129
VCAN_Nuc
FLNA_S2131
FLNA_Nuc
TNC_S72
TNC_Nuc
TOPORS_S98
TOPORS_S567
TOPORS_S570
TOPORS_Nuc
r ≥ 0.4
r ≤ −0.1
Control
4 hours
Day 1
Day 2
Day 3
Day 4
Day 5
Day 6
Day 8
Day 12
Z-scores
E
E/M
M
H
Structural model of MICAL3 p-sites, NLS and Importin-α
MICAL3 NLS
Importin-α
T684
S685
S687
I
Kinase activities during key stages and transition points
AKT1
CDK4
CHEK1
CSNK1G1
HIPK1
MAP2K1
MAP2K4
MAPK11
MARK1
PRKAA2
RPS6KA1
RPS6KA2
RPS6KB2
CSNK1G3
MAP2K6
ATM
PLK4
PIM1
CSNK1G2
ATR
NEK2
AURKB
AURKA
PLK1
MAK
NEK4
MARK4
CDK7
CSNK2A1
PAK1
RPS6KA3
AKT2
GRK5
GRK1
CAMK1
PRKCA
CDC42BPA
PRKDC
CSNK1E
CLK1
CAMK2A
CDK6
CLK2
CSNK1A1
EIF2AK2
IKBKB
MAPK8
MAPK9
MAPKAPK3
PDK2
PRKAA1
PRKCB
PRKCT
TTK
AKT3
CAMK2B
CDK2
CHUK
GSK3B
MAP2K5
MAPK13
MAPK14
PDHK4
PKD1
PRKCD
PRKCE
PRKCG
PRKCH
PRKCI
ROCK1
ROCK2
RPS6KB1
ARAF
CAMK4
CAMK2G
CSNK2A2
PDK1
RAF1
J
Expression profiles
PRKCA
Standardized expression (log2)
Mem
Nuc
WC
mRNA
PLC beta mediated events
Acetylcholine regulates insulin secretion
Apoptotic cleavage of cellular proteins
Initiation of Nuclear Envelope Reformation
Ca–dependent events
NOSTRIN mediated eNOS trafficking
DAG and IP3 signaling
XBP1(S) activates chaperone genes
Platelet sensitization by LDL
mTORC1–mediated signalling
Regulation of insulin secretion
Synthesis of IP3 and IP4 in the cytosol
CaM pathway
VEGFR2 mediated vascular permeability
Effects of PIP2 hydrolysis
Enrichment score
K
Expression profiles
AURKB
Standardized expression (log2)
Mem
mRNA
RHO GTPases activate IQGAPs
The NLRP3 inflammasome
CASP–mediated cleavage of cytoskeletal proteins
Sema3A PAK dependent Axon repulsion
Inflammasomes
Cell Cycle, Mitotic
Cell Cycle
Pathways associated with substrates
Enrichment score

Figure 7

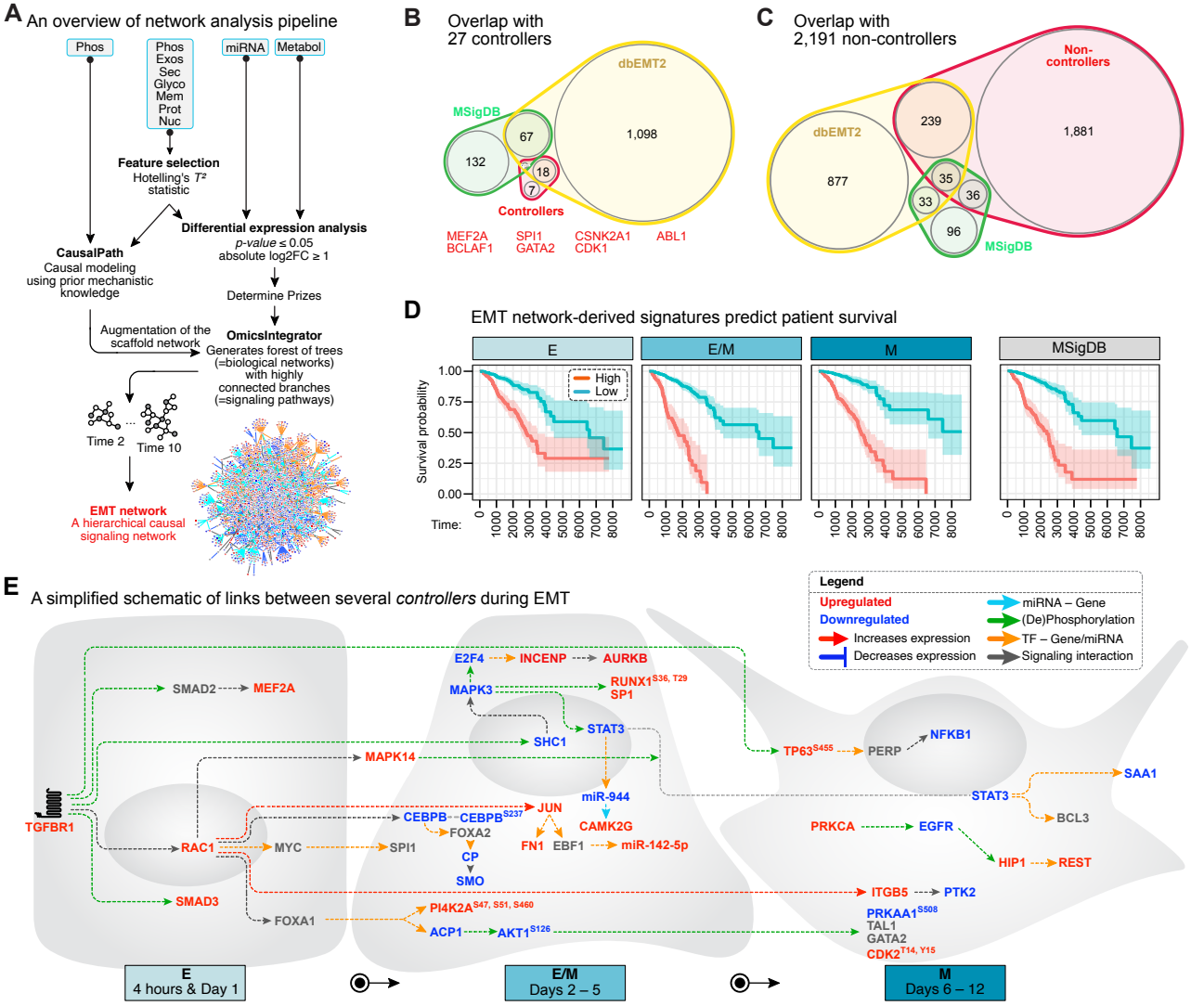
A
An overview of network analysis pipeline
Phos
Phos Exos Sec Glyco Mem Prot Nuc
miRNA
Metabol
Feature selection
Hotelling's T² statistic
Differential expression analysis
p-value ≤ 0.05
absolute log2FC ≥ 1
CausalPath
Causal modeling using prior mechanistic knowledge
Determine Prizes
Augmentation of the scaffold network
OmicsIntegrator
Generates forest of trees (=biological networks) with highly connected branches (=signaling pathways)
Time 2
Time 10
EMT network
A hierarchical causal signaling network
B
Overlap with 27 controllers
dbEMT2
MSigDB
132
67
1,098
18
7
Controllers
MEF2A
BCLAF1
SPI1
GATA2
CSNK2A1
CDK1
ABL1
C
Overlap with 2,191 non-controllers
Non-controllers
dbEMT2
239
1,881
877
35
33
36
96
MSigDB
D
EMT network-derived signatures predict patient survival
E
E/M
M
MSigDB
High
Low
Survival probability
1.00
0.75
0.50
0.25
0.00
Time:
0
1000
2000
3000
4000
5000
6000
7000
8000
E
A simplified schematic of links between several controllers during EMT
Legend
Upregulated
Downregulated
Increases expression
Decreases expression
miRNA – Gene
(De)Phosphorylation
TF – Gene/miRNA
Signaling interaction
E2F4
INCENP
AURKB
SMAD2
MEF2A
MAPK3
RUNX1S36, T29
SP1
STAT3
SHC1
MAPK14
TP63S455
PERP
NFKB1
SAA1
STAT3
BCL3
miR-944
TGFBR1
CEBPB
CEBPBS237
JUN
FOXA2
CAMK2G
FN1
EBF1
miR-142-5p
RAC1
MYC
SPI1
CP
SMO
PRKCA
EGFR
HIP1
REST
SMAD3
ITGB5
PTK2
FOXA1
PI4K2AS47, S51, S460
ACP1
AKT1S126
PRKAA1S508
TAL1
GATA2
CDK2T14, Y15
E
4 hours & Day 1
E/M
Days 2 – 5
M
Days 6 – 12
F
Workflow for morphometric analysis of inhibitor screen
Controllers
Selected Inhibitors
Experiment
Analysis
Inhibitor
Target
EMT inhibitor 1
Known EMT blocker
Sonidegib
SMO inhibitor
LB-100
PP2A inhibitor
Barasertib
AURKB inhibitor
Autocamtide
CAMK-II inhibitor
PP1
SRC inhibitor
APCP
NT5E inhibitor
TGFβ
+
Inhibitor permutations
Control
Day 3
GEN IMA SEG
Generic Image Segmentation Tool
Original
Segmented
Mask
Measured: Circularity of cells
G
Exposed combinatorial vulnerabilities
TGFβ/Control
1.00
0.66
0.33
0.00
EMT inhibitor 1
Sonidegib
LB-100
Barasertib
Autocamtide
PP1
APCP
H
3D biomimetic mammary duct-on-a-chip platform
DMSO
Day 0
Day 3
Soni + Auto
Day 0
Day 3
Day 3
DMSO
Soni + Auto
PI3Kα H1047R
Invasion Area
p-value = 0.0342
Area (μm²)
6e+05
4e+05
2e+05
DMSO
Sonidegib + Autocamtide
Invasion Distance
p-value = 0.0177
Average Distance (μm)
250
200
150
100
DMSO
Sonidegib + Autocamtide

Figure S1. Related to Figure 1

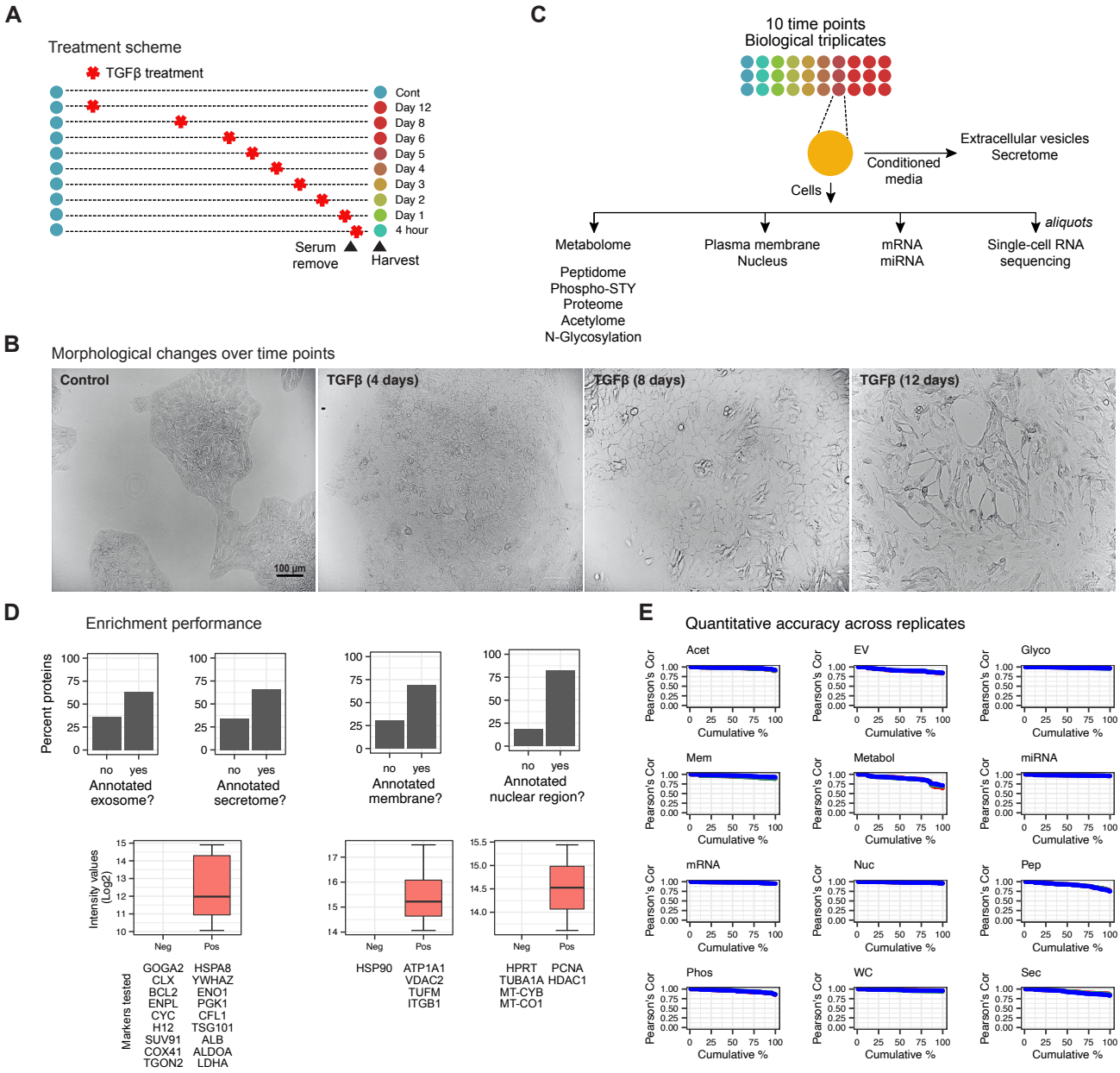

Figure S2. Related to Figure 2

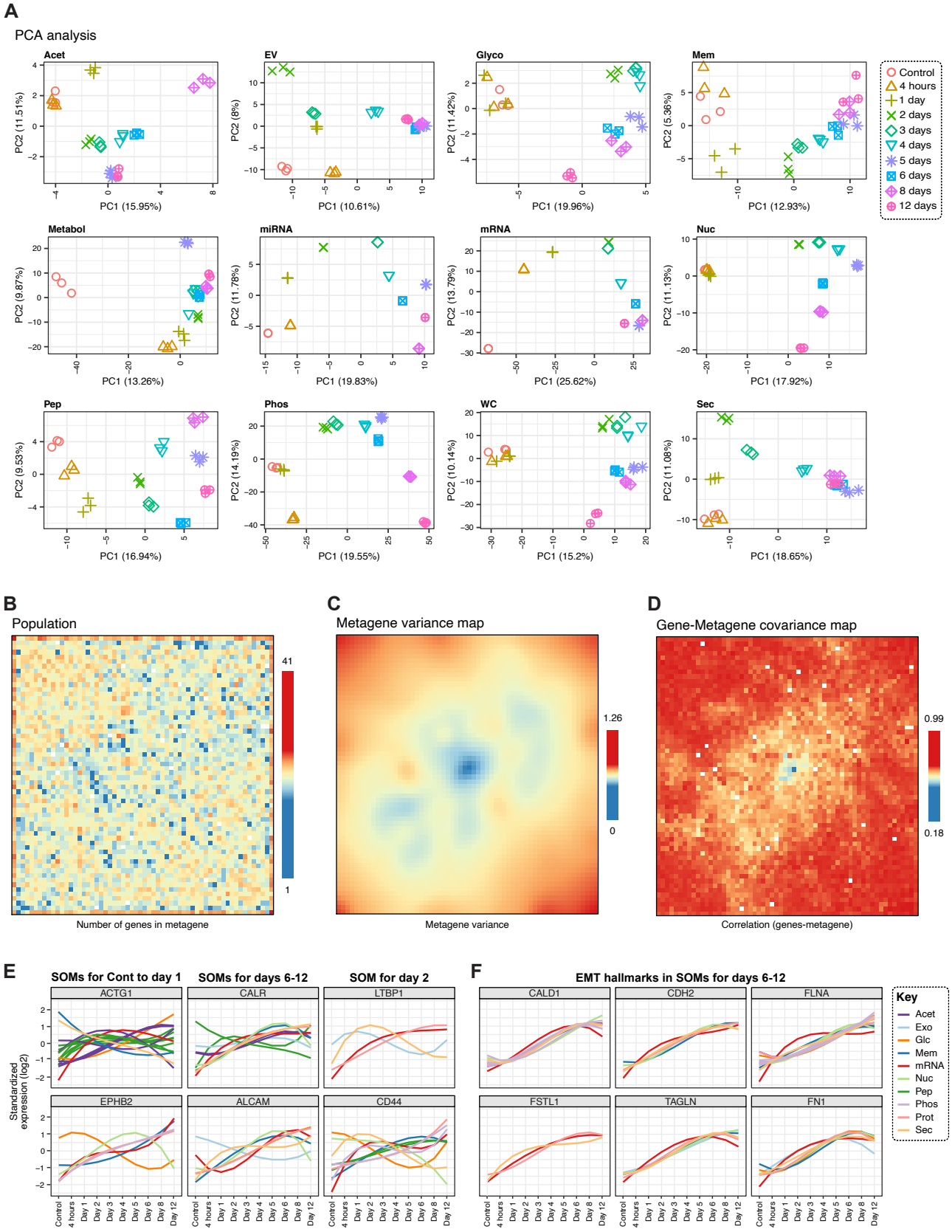

Figure S3. Related to Figure 3

A

GeneSet enrichment of metabolic pathways using active subnetworks

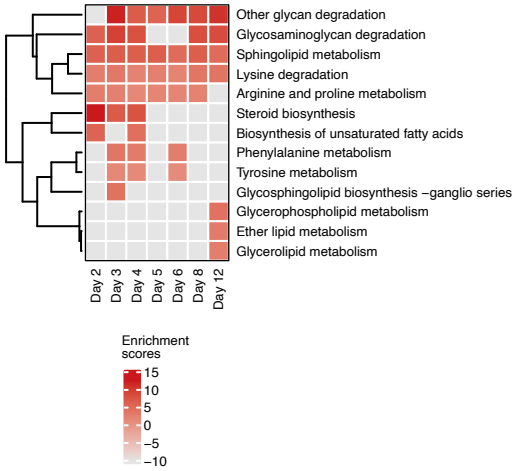

B

Metabolite-metabolite interaction network of metabolites identified in SOM for **4 hours to day 1**

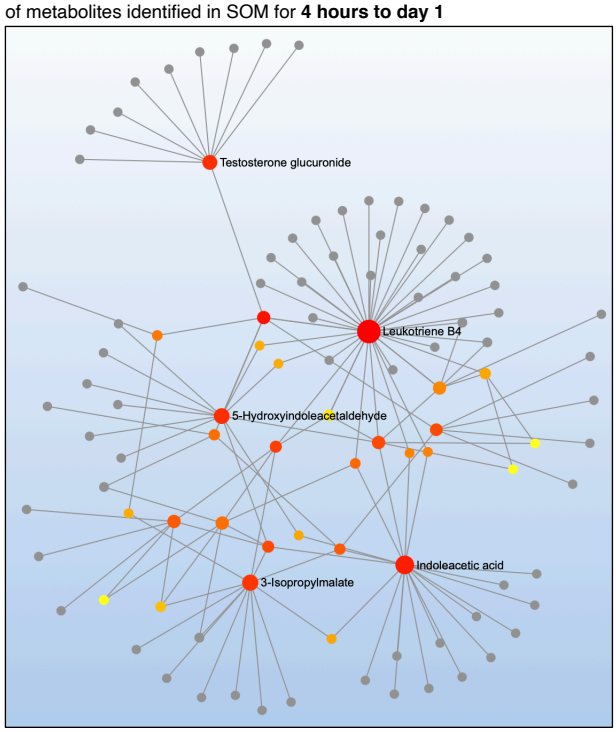

C

Metabolite-metabolite interaction network of metabolites identified in SOM for **day 2 to day 4**

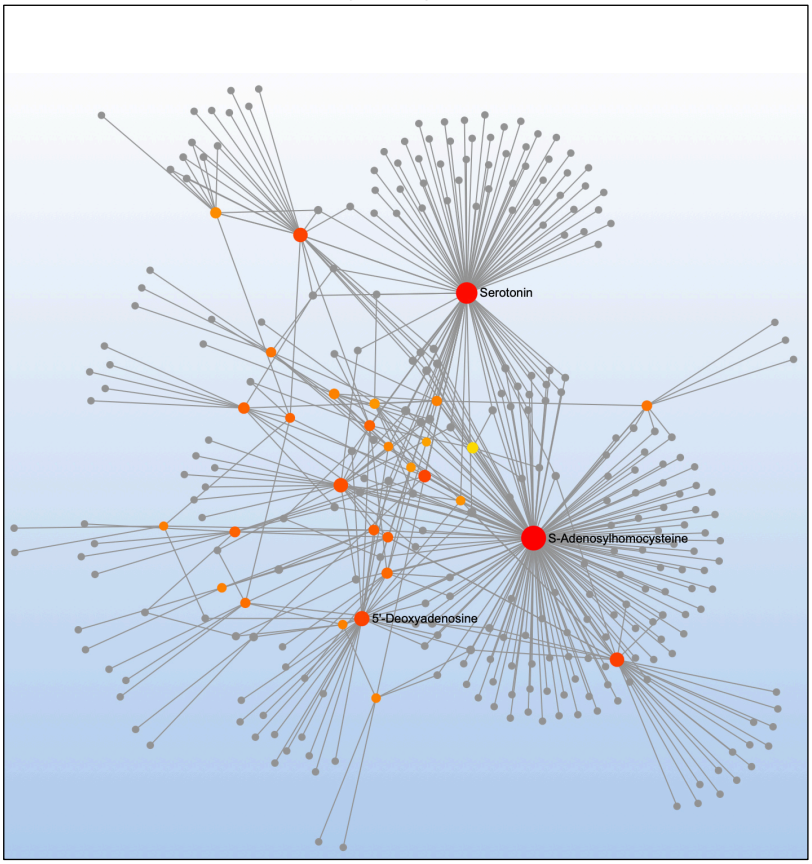

D

Metabolite-metabolite interaction network of metabolites identified in SOM for **day 5 to day 12**

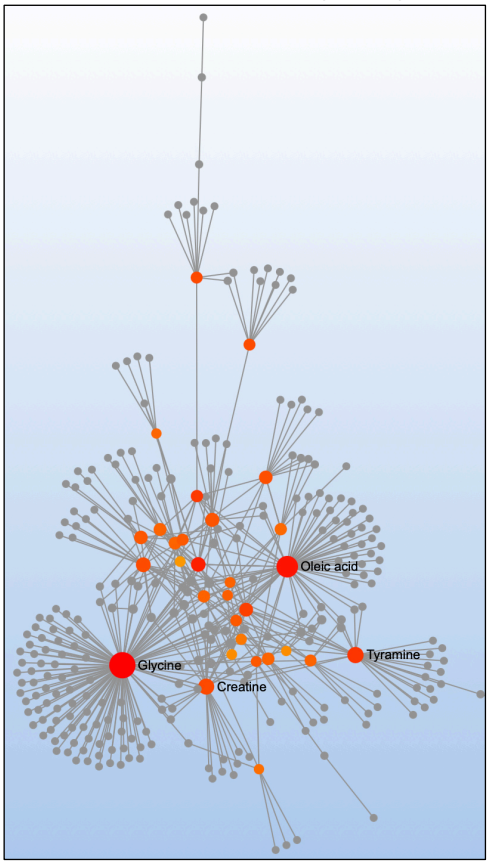

Figure S4. Related to Figure 4

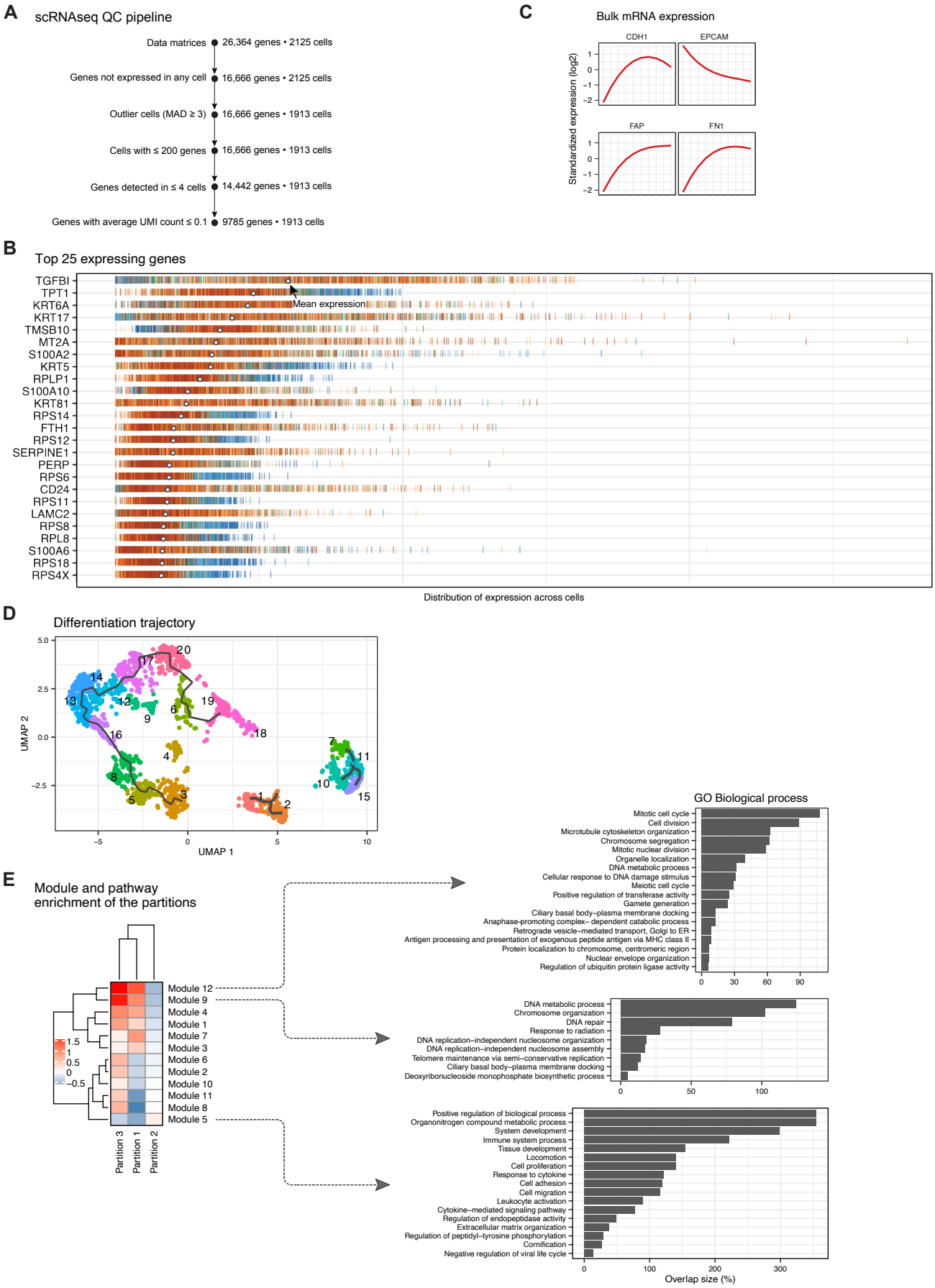

Figure S5. Related to Figure 5

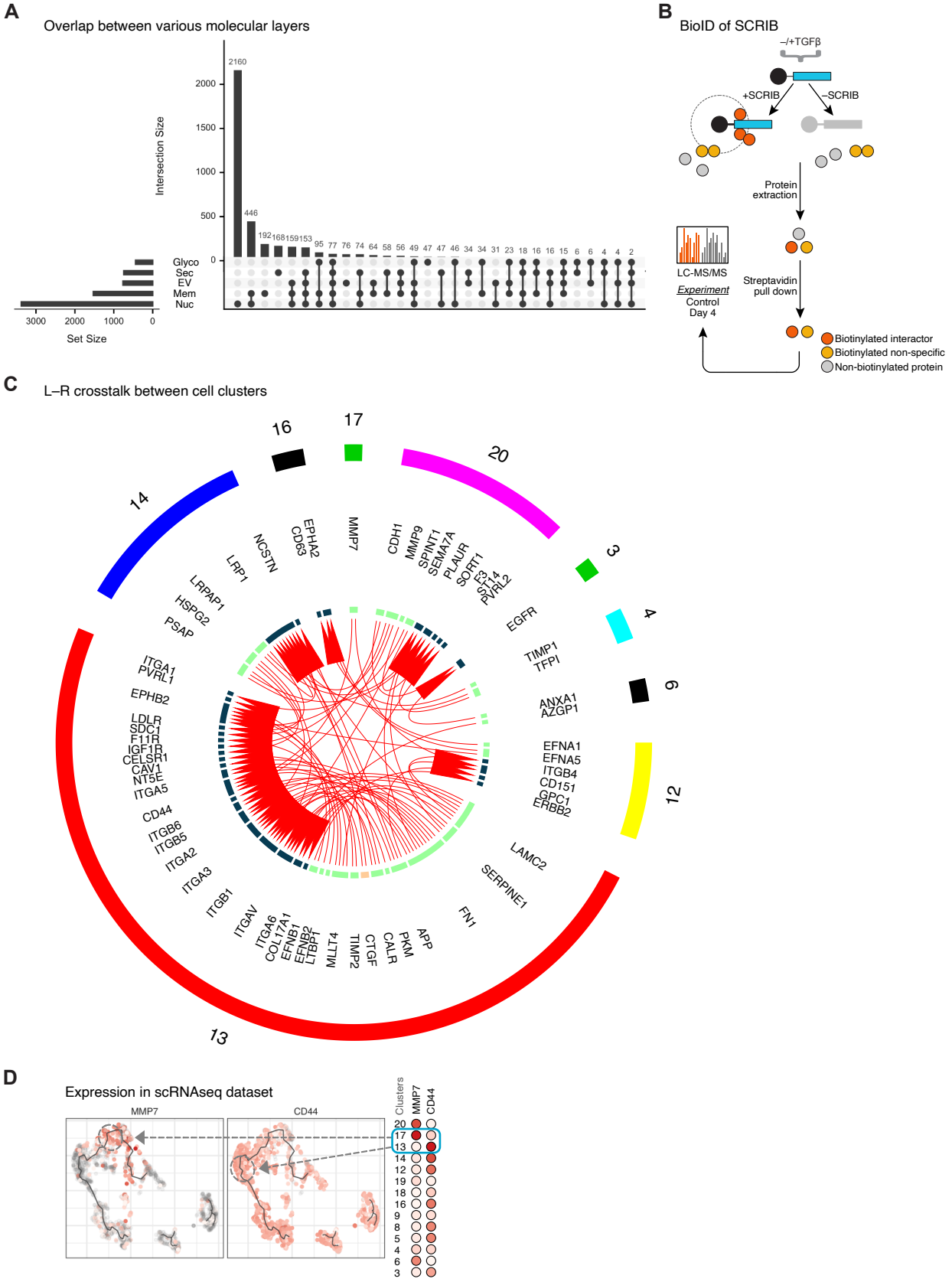

Figure S6. Related to Figure 6

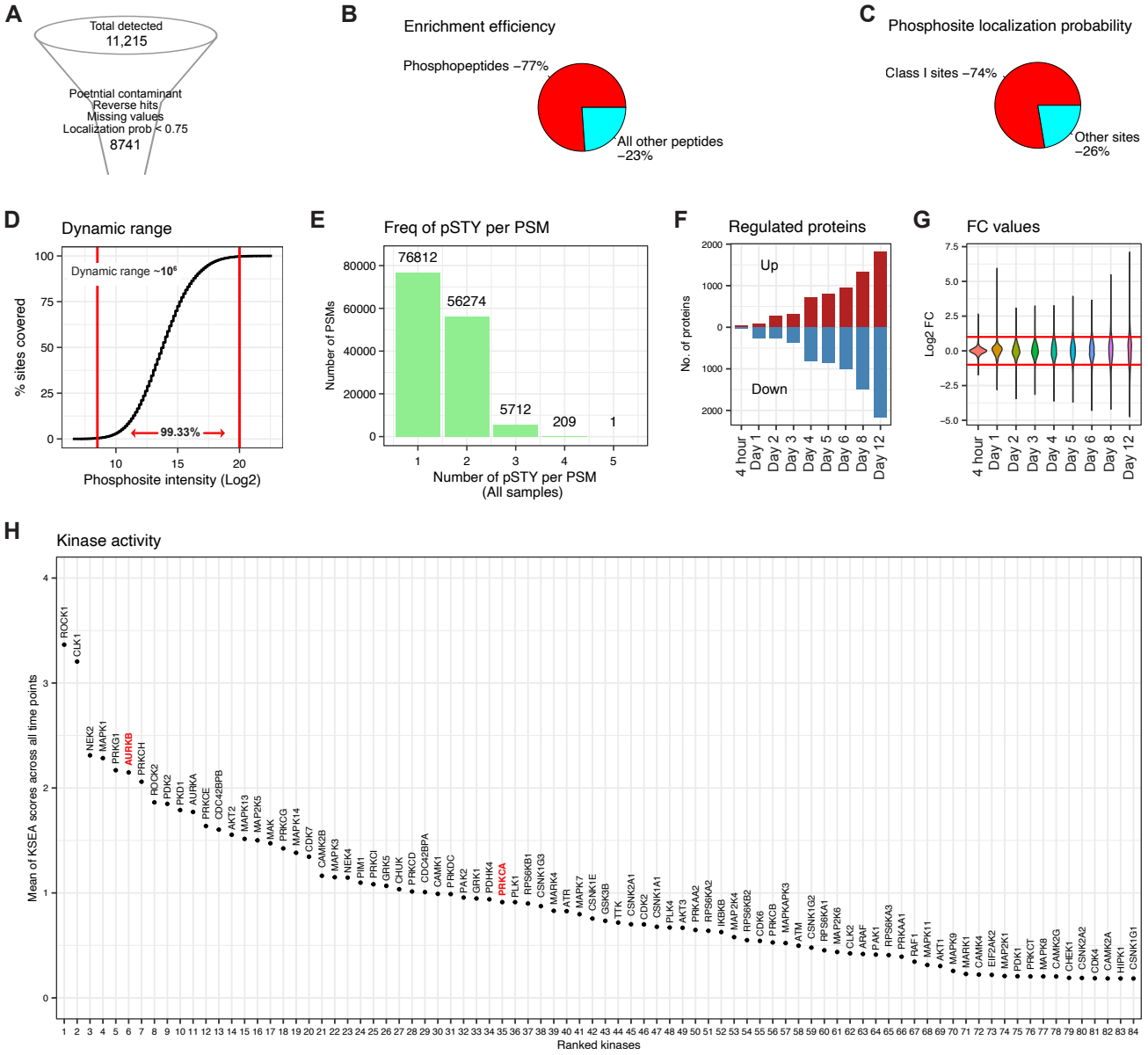

Figure S7. Related to Figure 7

A PathLinks: TGFBR1 to key EMT players

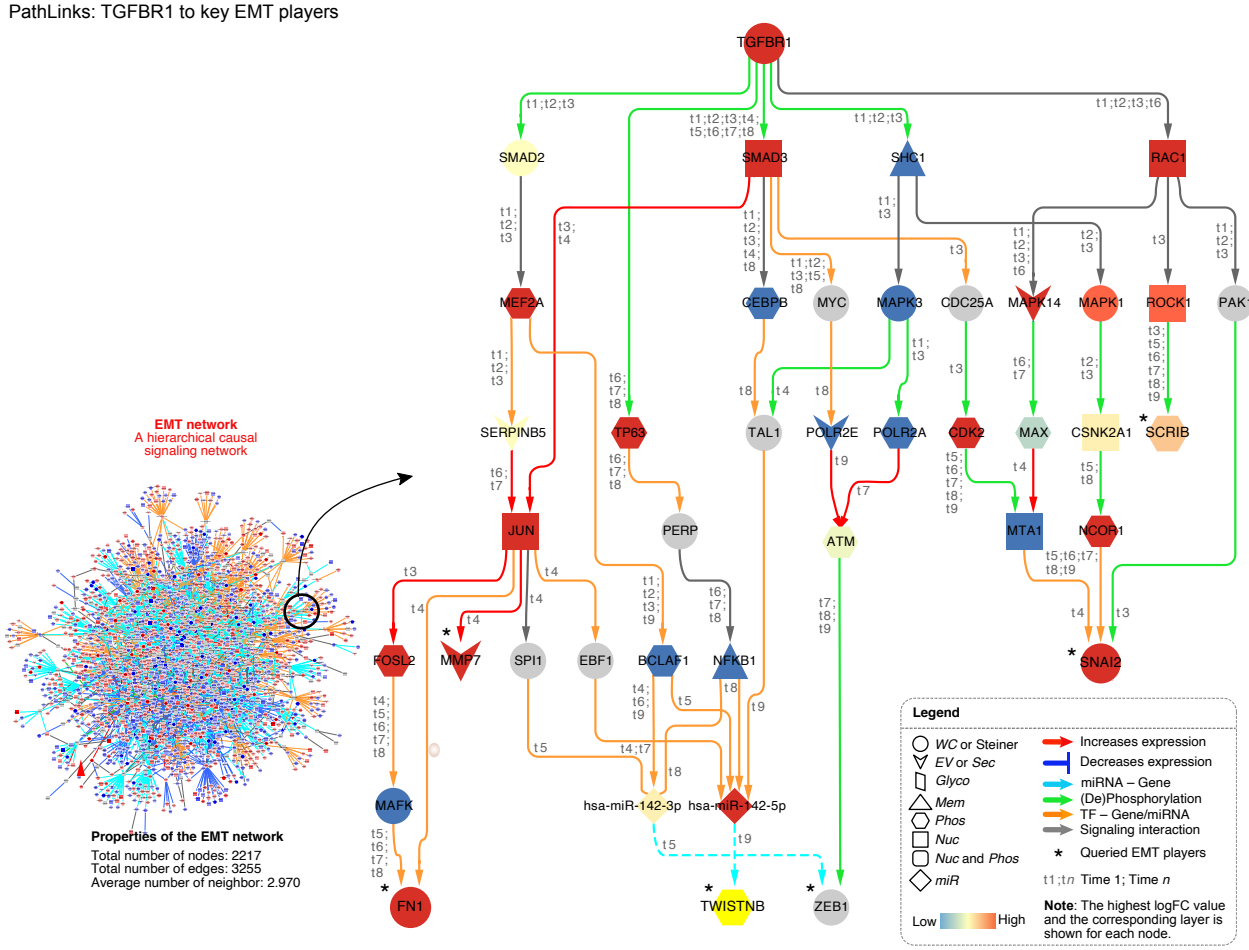
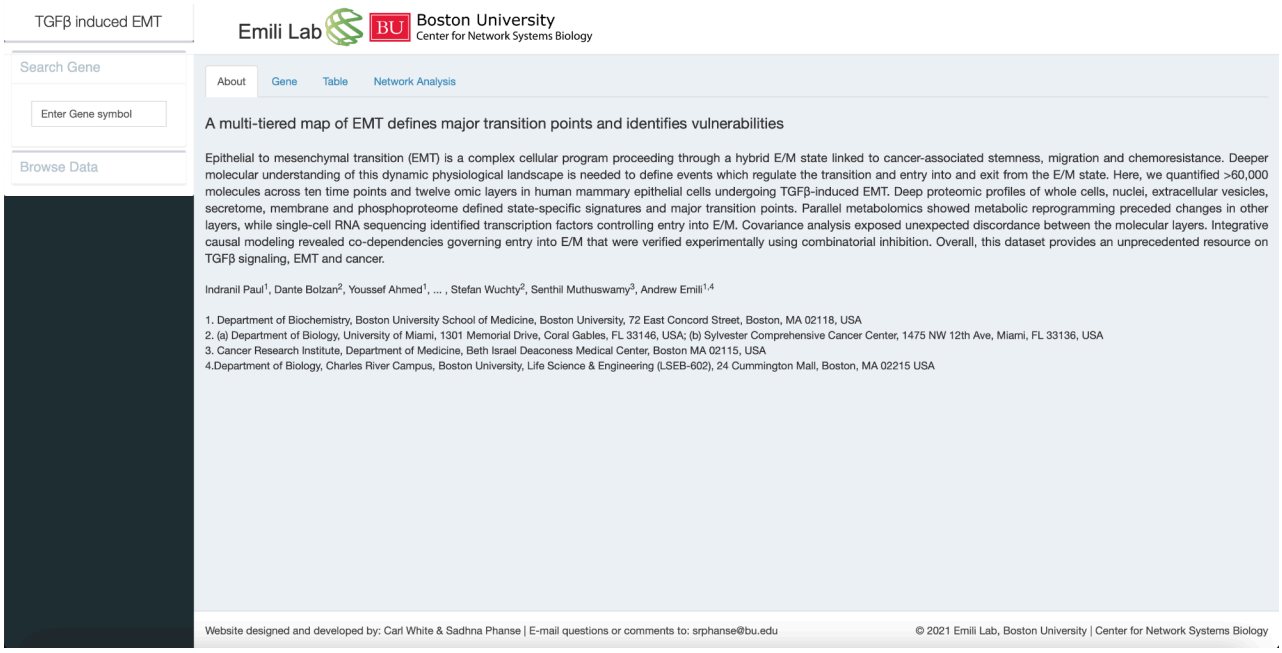
B EMT Website